12-22-2016

Reflection Matrix Method for Controlling Light After Reflection From a Diffuse Scattering Surface

Kenneth W. Burgi

REFLECTION MATRIX METHOD FOR CONTROLLING LIGHT AFTER REFLECTION FROM A DIFFUSE SCATTERING SURFACE

DISSERTATION

Kenneth W. Burgi, Major, USAF

AFIT-ENP-DS-16-D-011

DEPARTMENT OF THE AIR FORCE
AIR UNIVERSITY

AIR FORCE INSTITUTE OF TECHNOLOGY

Wright-Patterson Air Force Base, Ohio

AFIT-ENP-DS-16-D-011

REFLECTION MATRIX METHOD FOR CONTROLLING LIGHT AFTER REFLECTION FROM A DIFFUSE SCATTERING SURFACE

DISSERTATION

Presented to the Faculty

Graduate School of Engineering and Management

Air Force Institute of Technology

Air University

Air Education and Training Command

in Partial Fulfillment of the Requirements for the

Degree of Doctor of Philosophy

Kenneth W. Burgi, BS, MS

Major, USAF

22 December 2016

AFIT-ENP-DS-16-D-011

REFLECTION MATRIX METHOD FOR CONTROLLING LIGHT AFTER REFLECTION FROM A DIFFUSE SCATTERING SURFACE

DISSERTATION

Kenneth W. Burgi, BS, MS
Major, USAF

Committee Membership:

Dr. Michael A. Marciniak
Chairman

Maj Manuel R. Ferdinandus, PhD
Member

Dr. Mark E. Oxley
Member

Abstract

Dual photography is a technique capable of reconstructing an image of an occluded scene from reflected light by exploiting Helmholtz reciprocity. The primary limitation of dual photography is the line-of-sight requirement of the source used to illuminate the occluded scene. Complex radiometric modeling of multiple reflections allowed a technique called indirect photography to overcome the line-of-sight requirement of dual photography and recover some information from the hidden scene that was not directly visible from the camera or the light source.

This research focuses on reflective inverse diffusion, which was a proof-of-concept experiment that used phase modulation to shape the wavefront of a laser causing it to refocus after reflection from a rough surface. By refocusing the light, reflective inverse diffusion has the potential to eliminate the complex radiometric model of indirect photography by creating a virtual light source at the first diffuse reflector that satisfies the line-of-sight requirement of dual photography. However, the initial reflective inverse diffusion experiments provided no mathematical background and were conducted under the premise that the process operated similarly to transmissive inverse diffusion.

In this research, diffraction modeling of the reflective inverse diffusion experiments led to the development of Fourier transform-based simulations. Simulations and experimentation were used to develop reflection matrix methods that determine the proper phase modulation to refocus light after reflection to any location in the observation plane. These techniques provide a new method for controlled illumination of an occluded scene that can be used in conjunction with dual photography. This document provides the mathematical background for reflective inverse diffusion, the reflection matrix methods for phase modulation, and describes the simulations and experiments conducted.

For my family

Acknowledgements

I would like to extend my deepest appreciation for my faculty advisor, Dr. Michael Marciniak. His guidance over the years was invaluable and this research would not have been possible without his support. I would also like to extend my thanks to Dr. Mark Oxley and Dr. Stephen Nauyoks for their support and mentoring. Special thanks to Mr. Mike Ranft and Mr. Greg Smith for their technical expertise and laboratory support throughout this research effort.

Kenneth W. Burgi

Table of Contents

Page

List of Figures

List of Tables

List of Acronyms

AFIT Air Force Institute of Technology

DMD digital mirror device

LCoS liquid crystal on silicon

SLM spatial light modulator

HeNe helium-neon

CCD charge-coupled device

NPBS non-polarizing beam splitter

BNS Boulder Nonlinear Systems

FFT fast Fourier transform

RM reflection matrix

DMD digital micro-mirror device

FWHM full-width-at-half-maximum

RMS root mean square

NPBS non-polarizing beam splitter

DDDAS dynamic data driven applications systems

REFLECTION MATRIX METHOD FOR CONTROLLING LIGHT AFTER REFLECTION FROM A DIFFUSE SCATTERING SURFACE

I. Introduction

The Helmholtz Reciprocity Theorem [1] describes the symmetric nature of light propagation. This theorem states that the effect measured at location P from a point source at location P_0 would be the same as the effect measured at P_0 from an equivalent point source located at P. Dual Photography [2] is a technique that takes advantage of Helmholtz reciprocity. The process involved a scene illuminated by a digital projector pixel by pixel. A digital camera then recorded the reflected light from the scene for each pixel illumination. Using this information, a transport matrix was produced to relate the effects of the projector pixels to the camera pixels. The transport matrix can be used to mathematically interchange the positions of the camera and the projector producing a view of the scene from the position of the projector as if it were illuminated from the position of the camera. This allowed recovery of scene information that was only visible from the projector's point of view [2].

Scene information hidden from the camera but recovered using dual photography must be visible from the viewpoint of the projector. This requirement limits its usefulness outside the author's original work of capturing and relighting scenes. In other words, if the desired image is observable from the viewpoint of the projector, then the simplest solution would be to place a camera there. Indirect photography [3, 4] is a method, developed at the Air Force Institute of Technology (AFIT), to remove the line-of-sight requirement of dual photography and recover scene information not

directly visible from the position of the camera or projector. This would allow the light source, now a laser, and the camera to be co-located and yet still retain the ability "to see around corners." This was accomplished through radiometric modeling of multiple diffuse reflections. Indirect photography was successful at recovering some hidden scene information after two diffuse reflections. Initial methods for indirect photography limited reflections to forward scattering only [3, 4].

Indirect photography illuminates a scene with reflectively scattered light. Since the illumination pattern no longer provides a controlled canonical basis, as with dual photography, the ability to construct a proper transport matrix to image the occluded scene is significantly impaired. Adaptive optics techniques, such as phase modulation, can be implemented to compensate for the reflective scattering of the illumination source. The ability to control the illumination source and refocus light after reflection would reduce the indirect photography problem back to that of dual photography and allow proper construction of a transport matrix for imaging the hidden scene.

Transmissive inverse diffusion [5–8] is a method for refocusing light after being scattered by transmission through a turbid medium. Reflective inverse diffusion is developed in this research. The details of reflective inverse diffusion will be discussed in Chapter II. Applying the concept of inverse diffusion to indirect photography, refocusing light from the first diffuse reflection, has the potential to simplify the method back to that of dual photography. From the observation plane perspective, the origin of the light source is the first diffuse reflector, thus satisfying the line-of-sight requirement of dual photography.

Reflective inverse diffusion was a proof-of-concept research at AFIT. Phase modulation was employed to shape a plane wave prior to reflecting off a diffuse surface. Phase modulation was achieved via a liquid crystal on silicon (LCoS) spatial light modulator (SLM). The results showed that a properly modulated plane wave could

be focused to a tight spot after reflection. The SLM also demonstrated some degree of control over the location of the focus spot in the observation plane [9].

The purpose of this research is to develop a method of controlled illumination using reflectively scattering light that could be used in conjunction with dual photography to allow imaging around corners. This method required significant advancement of the theory and application of reflective inverse diffusion. The proof-of-concept experiments were based on methods developed for transmissive inverse diffusion. Both transmissive inverse diffusion and the original experimental results for reflective inverse diffusion are covered in Chapter II. Diffraction-based models were developed to provide the basis for simulations of reflection inverse diffusion and are presented in Chapter III. The reflection matrix (RM) was developed to provide the necessary control of the reflected light. The relationship between every segment of the SLM and every segment of the charge-coupled device (CCD) detector is contained in the RM. The algorithm used to measure and construct the RM is covered in Chapter IV. The experimental optical setup and reflector material surface properties that effect the performance of the RM are examined in Chapter V. Finally, initial methods of reconstructing an RM from partial data and expanding an existing RM to cover an observation plane larger than that measured are presented in Chapter VI.

II. Background

The concept of reflective inverse diffusion was based on methods developed for refocusing light through thin films of a turbid medium. When coherent light is transmitted through a stationary diffuser (i.e. a turbid medium), a fine granular intensity pattern is formed called speckle [10]. The speckle is caused by the individual path length differences imparted by the medium to different portions of the coherent light. Thus, transmissive inverse diffusion uses phase modulation to conjugate the phase changes imparted by the turbid medium and causes the light to refocus after transmission.

Speckle can also be produced from coherent light reflecting off a rough surface. The path length differences that produce the speckle are caused by the surface height deviations of the material [10]. A rough surface, in the context of optics, is any material with a surface height standard deviation on the order of a single wavelength of light (λ) [11]. Due to the similarities between transmissive and reflective speckle, reflective inverse diffusion methods were initially based on the phase modulation techniques used in transmissive inverse diffusion.

2.1 Transmissive Inverse Diffusion

Driven by potential medical applications of imaging through tissue, inverse diffusion was first accomplished in transmission by focusing light through a turbid medium. Vellekoops's method exploited the linearity of the scattering process [5]. The experimental set-up for transmissive inverse diffusion is shown in Figure 1. The turbid medium is placed between two microscope objectives. The first microscope objective applies a demagnified image of the modulated beam from the SLM onto the turbid medium. The second objective collects the transmitted scatter pattern and provides

a magnified image on the CCD detector that provides feedback for the system.

Both the SLM and CCD are addressed in segments and each segment consists of multiple pixels. The basic iterative algorithm for transmissive inverse diffusion selects one segment of the CCD and seeks to maximize the intensity at that location. The phase of each of the SLM segments is cycled through a small subset of the available $[0, 2\pi]$ range until the maximum intensity at the CCD target segment is achieved.

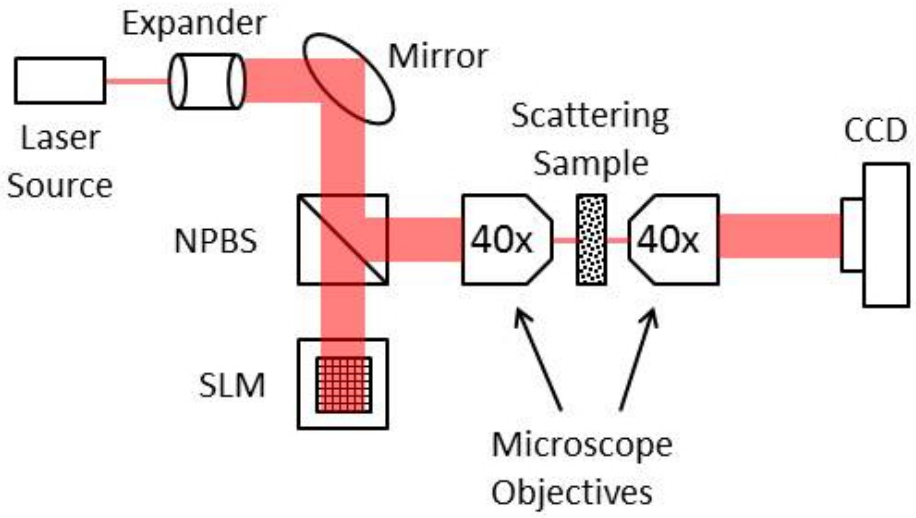

Figure 1. Optical setup for transmissive inverse diffusion. A microscope objective is used to demagnify the modulated beam and image it onto the scattering medium. The transmitted scatter pattern is magnified by a second microscope objective and image onto the feedback CCD.

The transmitted field at the m^{th} segment of the observation plane is given by,

$$E_m = \sum_{n=1}^{N} t_{mn} A_n e^{j\phi_n} \tag{1}$$

where t_{mn} represents the mn^{th} element of the complex-valued transmission matrix, and $A_n e^{j\phi_n}$ is the field from the n^{th} segment of the SLM. The source field is segmented by the modulator into N segments and transmitted through the scattering medium. The field in the observation plane consists of a linear combination of these N segments

of the source field at each of the m observation positions [5]. Normalizing equation (1) to intensity, $A_n = {}^1/\sqrt{N}$, and the observed intensity at the m^{th} segment is then

$$I_m = |E_m|^2 = \frac{1}{N}\left|\sum_{n=1}^{N} t_{mn} e^{j\phi_n}\right|^2 . \tag{2}$$

Intensity enhancement is a measure of performance for transmissive inverse diffusion and was defined by Vellekoop as [7],

$$\eta = \frac{\langle I_{opt}\rangle}{\langle I_{rnd}\rangle}, \tag{3}$$

which is a simple ratio of the average intensity of the optimized spot $\langle I_{opt}\rangle$ divided by the average intensity of the unoptimized random speckle $\langle I_{rnd}\rangle$ [6]. Each grain of speckle in the intensity pattern is the sum of a large number of individual light paths through the medium. Applying the Central Limit Theorem, the distribution of the individual paths through the medium is approximated by a Gaussian [12]. Assuming the paths through the material are independent, the real and imaginary components of the turbid medium become individually Gaussian, then this distribution is known to be a circular Gaussian [13]. Thus, for transmission through a random medium, the t_{mn} terms follow a statistically independent complex circular Gaussian distribution [13] with properties that can be used to simplify equation (3) and express the ideal intensity enhancement, $\eta_{transmissive}$, as a function of the total number of SLM segments [7],

$$\eta_{tranmissive} = \frac{\pi}{4}(N-1) + 1 \approx \frac{\pi}{4}N. \tag{4}$$

2.2 Transmission Matrices

Matrix multiplication has been used to represent the linear combination of N segments of the modulator from Vellekoop's method. The transmission matrix, $\mathbf{T}$, approximates the effects of scattering by the medium and propagation through the system. Several methods for experimentally determining the transmission matrix all rely on orthogonal Hadamard or Walsh-Hadamard basis vectors [14–16]. Recently, methods for determining transmission matrices using the temporal Fourier transfrom of instensity measurements have been developed [17]. The advantage of the matrix approach is the ability to use the transmission matrix to determine the input field for any desired output.

2.2.1 Other Literature.

Iterative methods for transmissive inverse diffusion were developed by Vellekoop and Mosk [7]. In general, these methods show a linear improvement in the enhancement of the tightly focused spot with an increase in the number of segments of the modulator. Optimization for a single SLM segment took 1.2 seconds [5]. However, it is estimated that a single segment optimization of 1 millisecond is needed to make dynamic measurements in biological tissue [5–8, 18]. This optimization time has been achieved by using acousto-optic modulators to rapidly scan for the optimum phase before applying it to the relatively slow SLM. Feedback time was reduced by using a simple photo-diode for intensity measurements in the observation plane [19]. Phase modulation has also been used to maximize the transmission of light through scattering media without focusing it to a single spot [20].

Transmission-matrix approaches were soon developed beyond the iterative methods [15, 21]. These methods tend to be favored over iterative methods as they allow for control of the light in the observation plane without need to rerun a sometimes

lengthy iterative algorithm. Several methods for measuring the transmission matrix involve using the Hadamard orthonormal basis vectors to interrogate the scattering sample [15, 16, 21]; however, more recent publications allow for any orthogonal basis to be used [17]. Statistics and control capabilities of transmission matrices have been examined in detail [22]. Most wavefront-shaping methods favor phase modulation; however, methods for determining the transmission matrix of a scattering medium have been developed using binary amplitude modulation with digital micro-mirror devices (DMDs). These devices operate in the 20 kHz range much faster than the 30-60 Hz of liquid crystal on silicon (LCoS) spatial light modulators (SLMs) [14, 23]. Background speckle tends to be higher for images generated using transmission matrices due to errors in transmission matrix measurement and estimation process; however, there are published methods for reducing this side effect [24].

Transmissive inverse diffusion has been used to image through scattering material [25, 26]. Imaging through biological tissues along with other applications in biophotonics have also been explored [27]. Transmission matrix methods have also been used to determine the polarization state of incident light [28]. Wavefront shaping methods using phase modulation were used to create a programmable optical circuit using scattering materials [29]. The ability to control the propagation time [30] and change the direction of propagation in scattering media [31] has also been demonstrated. Both Mosk and Vellekoop recently published summaries covering most of the new techniques for transmissive inverse diffusion using wavefront shaping [32, 33], where it was mentioned that the transmission matrix approach could be applied to any linear process without loss of generality, including reflection.

2.3 Reflective Inverse Diffusion

2.3.1 Experimental Set-up.

The experimental set-up for reflective inverse diffusion was adapted from that of transmissive inverse diffusion shown in Figure 1. Although similar, the two have significant differences. In transmission, microscope objectives are located on both sides of the scattering medium. To have optical elements this close to the scattering medium is not practical for use in reflection, and is also an impractical requirement for imaging around corners [9].

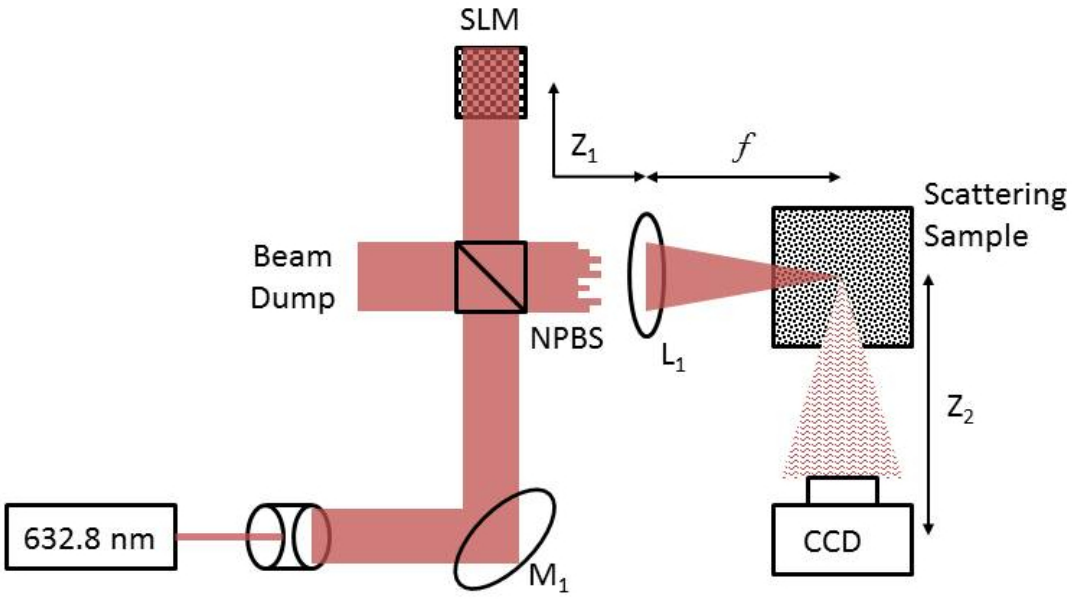

Figure 2. Focal plane optical setup for reflective inverse diffusion. A vertically polarized HeNe laser is expanded, collimated, and normally incident on the SLM. The phase modulated beam is then focused onto the rough surface reflector with positive lens (L_1) and the reflected speckle pattern is recorded by the CCD. The mirror (M_1) and the non-polarizing beam splitter (NPBS) are used to allow normal incidence with the SLM. For focal-plane experiments and simulations, the lens focal length, f, is 500 mm, and the distances Z_1 and Z_2 are 15 ± 0.5 cm and 50 ± 0.5 cm, respectively.

The original proof-of-concept experiment for reflective inverse diffusion (shown in Figure 2) was done with a 5 mW HeNe laser (632.8 nm wavelength) linearly polarized

with the vertical axis of the SLM. The beam was then expanded and collimated. A non-polarizing beam splitter (NPBS) allows normal incidence onto the SLM. The modulated beam was focused onto the diffuse reflector using a 500-mm positive lens. The focused beam is incident on the reflector at 45°, the reflector then scatters the beam onto the CCD detector [9].

2.3.2 Algorithm.

The algorithm for reflective inverse diffusion was adapted from transmissive inverse diffusion, a method for focusing light after transmission through a diffuse media. The basic algorithm measures the intensity in the observation plane while incrementally adjusting the phase of the SLM pixel. The phase value that produced the highest intensity spot in the observation plane was selected, and the algorithm moved to the next pixel [5, 9].

The SLM, used in the experiment, was a Boulder Nonlinear Systems (BNS) model P512 with a resolution of 512-by-512 pixels. Each pixel was 15μm square, and capable of 256 discrete phase levels with a total phase stroke of 2π. The SLM is therefore capable of 2^{26} ($\approx 10^8$) different phase screens. Since it is impractical to test all possible pixel/phase combinations, the SLM was further grouped into 16-by-16 pixels blocks to be modulated as a single super pixel; the resolution of SLM would then be 32 by 32 super pixels. Each super pixel was phase modulated from 0 to 2π in increments of $\frac{\pi}{10}$ for a total of 21 possible phase values [9].

The algorithm is forward only; once a super pixel is optimized, it moves to the next super pixel. The algorithm never determines if the new phase value for the current super pixel affects any of the previously optimized super pixels. Since the SLM is phase only, the effects of modulating a single super pixel are not independent of each other. It can be shown that with a single pass through, the algorithm does

not produce a unique solution, and that the solution depends on the initial values of the SLM pixels.

Looping through the algorithm does improve spot intensity, and reduces background speckle; however, it is very time consuming. Coarse pre-optimization was employed as a compromise between spot enhancement and processing time. The SLM is initially segmented into 2-by-2 blocks, each consisting of 256-by-256 pixels. Each block is optimized to one of the 21 phase values. The SLM is then be segmented into 4-by-4 blocks and optimized to one of the 21 phase values. This process of course optimization is repeated until the SLM is segmented into the 32-by-32 super pixels [5, 9].

The initial algorithm sought to improve efficiency by under-filling the SLM, and only modulating the pixels illuminated by the laser. This only produced marginal reductions in processing time, but added the uncertainty of laser alignment. It would be impossible to determine if some SLM pixels were illuminated by the laser, but left unmodulated. The end result of the algorithm was 1,160 super pixel optimizations for each experiment. Each super-pixel optimization takes approximately 32 seconds to process. The total process took over 10 hours to complete [9].

2.3.3 Summary of Results.

The original proof-of-concept experiments for reflective inverse diffusion measured the enhancement from six different scattering materials: Spectralon®, brushed aluminum, sandblasted aluminum, Infragold®, white paint on glass, and graphite. The reflector materials were selected based on the differences in scattering properties. The surface roughness of the samples was measured and compared with the reflected spot enhancement, and the final full-width-at-half-maximum (FWHM) spot size produced by the algorithm. These measurements are shown in Table 1.

Table 1. Summary values of enhancement, surface roughness, and spot size for each of the six reflective samples measured and the one transmission sample.

Reflective Samples	Enhancement (η)	Roughness (R_{rms})	Final FWHM
Brushed Aluminum	122.3	1.5 μm	36 $\pm$ 3 μm
Infragold®	89.9	9.4 μm	38 $\pm$ 3 μm
Sandblasted Aluminum	67.7	2.3 μm	38 $\pm$ 3 μm
Graphite	37.3	3.5 μm	41 $\pm$ 3 μm
White paint	36.8	1.7 μm	41 $\pm$ 3 μm
Spectralon®	13.8	Unprofiled	45 $\pm$ 3 μm
Transmissive Sample			
White paint	56.4	1.7 μm	63 $\pm$ 3 μm

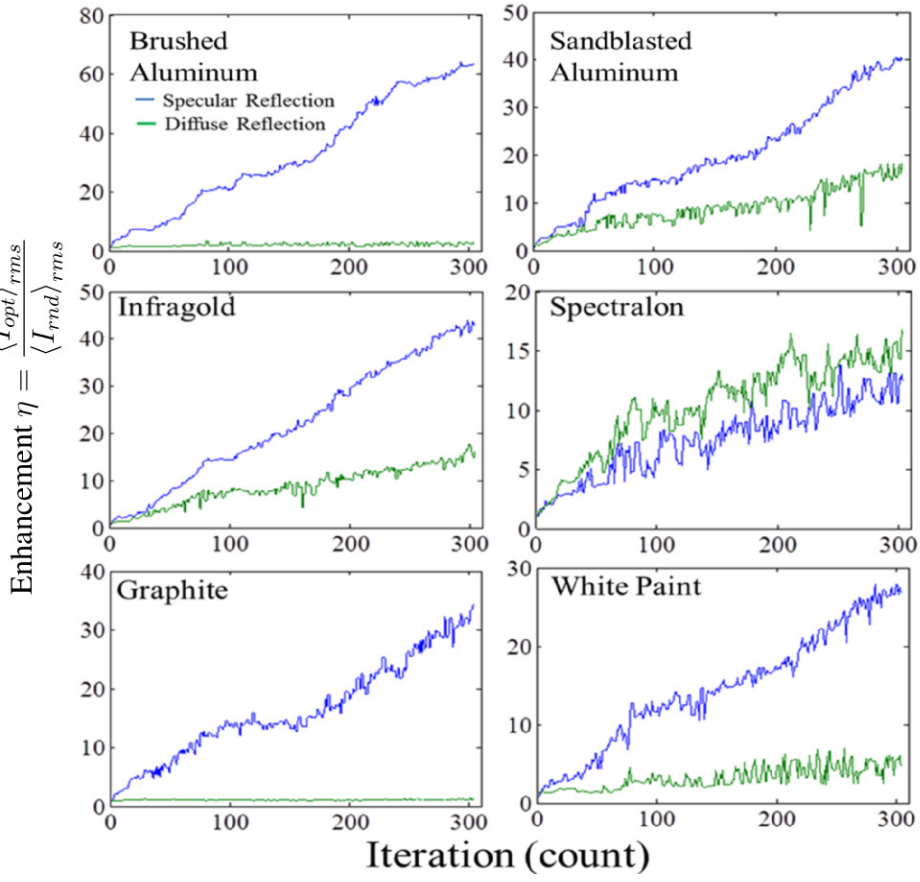

Figure 3. Enhancement comparisons of specular and diffuse regions of reflection. Enhancement is plotted after each optimization with the CCD placed in the specular region at 45° from the reflector surface normal (blue). Specular is defined as a reflection angle of $45^\circ \pm 0.5^\circ$ from the surface normal. Diffuse is defined as 15° off specular.

The brushed aluminium reflector produced the highest level of enhancement the initial background speckle intensity. All of the diffuse reflectors used in the original experiment showed at least an order of magnitude enhancement in the focused spot for $N = 1,024$. The original experiments also demonstrated, using the iterative optimization algorithm, that the focused spot in the observation plane could be positioned anywhere within the CCD, displaced up to 8.3 mm diagonally, at a distance of 50 ± 0.5 cm from the reflector, and experienced less than a 13.5% drop in peak intensity of the focused spot. When the diagonal distance is increased to 108.2 mm, the peak intensity of the spot is decreased by 58.6%. Using these diagonal displacements, the specular region was defined with an angle of incidence and angle of reflection equal to $45^\circ \pm 0.5^\circ$ and the diffuse region was defined as 15° off specular. Figure 3 shows the enhancement achieved by each material for the specular and diffuse regions. The final optimized SLM for Figure 3 contained $N = 256$ segments, but with pre-optimization the total process performed 340 segment optimizations. Figure 3 also shows that highly reflective materials that are strongly scattering (i.e. less specular) maintained enhancement better at larger displacements of the focus spot than did the more specular samples [9].

The speckle pattern produced by a fixed SLM phase map and diffusely reflecting sample varied with time. The decorrelation of the speckle pattern is a function of both the material properties of the diffuse reflector and the laboratory test conditions. The correlation coefficient was plotted with time for the brushed aluminum, Spectralon®, and transmissive white paint samples, and is shown in Figure 4. As expected, the metal reflectors maintained a much higher correlation coefficient. Thus, most of the decorrelation for the metal reflectors is attributed to the changing environmental conditions of the laboratory, such as temperature, air currents from the laboratory ventilation system, minute mechanical vibrations, and device measurement error and

noise.

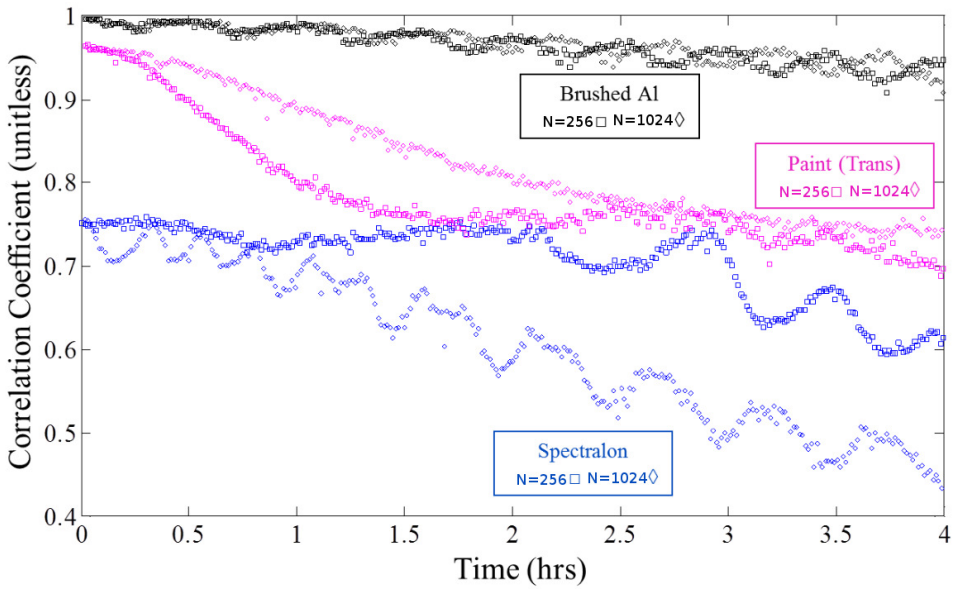

Figure 4. The correlation coefficient of the speckle pattern produced by an unoptimized phase map of as a function of time. The unoptimized phase map applied to the SLM consisted of N equal-sized segments of random phase values arranged in a square. The correlation coefficient for $N = 256$ and $N = 1024$ are shown for the brushed aluminum, transmissive white-paint-on-glass, and Spectralon® samples. Reprinted with permission [9].

Previous work in the transmissive inverse diffusion showed enhancements (η) ranging from 50 to 1,000 using both iterative and transmission-matrix methods [6, 14, 19, 21, 34]. The cause of this wide range of enhancement values is still currently being investigated, with some of the disparity likely attributed to noise [34]. The volumetric scatterers, such as Spectralon® and white-paint samples, showed a much higher degree of decorrelation compared to the metals. This decorrelation over time adds a degree of uncertainty to the process, where previously optimized SLM segments are in fact suboptimal by the time the process is complete. These suboptimal segments cause a decrease in the overall spot enhancement [9].

2.4 Summary

Path-length difference is the main cause of the light scatter and resultant speckle intensity patterns in both transmissive and reflective inverse diffusion. In the transmissive case the path-length difference is caused by the large number of random paths through the turbid medium. In the reflective case, the path length differences are caused by the wavelength-sized surface height fluctuations of the material. Ultimately, path-length differences are expressed as phase differences in the light field and can therefore be compensated for through phase modulation.

The proof-of-concept experiments for reflective inverse diffusion provided no mathematical models or simulations. The experiment assumed the ideal enhancement performance was comparable if not equal to the transmission case. A diffraction-based model is developed in Chapter III and surface statistics are used to develop an expression for the ideal enhancement for reflective inverse diffusion.

III. Mathematical Model for Reflective Inverse Diffusion

In this chapter, rough surface models with Gaussian-distributed surface height fluctuations are used to derive an expression for ideal enhancement for reflective inverse diffusion. The original reflective inverse diffusion experiments took over 10 hours to optimize the SLM phase map of $N = 1,024$ segments so that it refocused light to a single CCD segment [9]. A mathematical model to drive numerical simulations was needed to further develop reflective inverse diffusion. Such a model is also developed in this chapter.

3.1 Enhancement for Reflective Inverse Diffusion

Light scattering, whether by transmission through or reflection from a medium, is a linear process. Despite complexity and unknown material properties, it can be considered deterministic as long as the medium is static [33]. Therefore, the relationship developed for transmissive inverse diffusion for the observed total field in the target area is also valid for the reflective case. The field at the m^{th} position was given in Equation (1) [5], repeated here as

$$E_m = \sum_{n=1}^{N} t_{mn} A_n e^{j\phi_n}, \tag{1}$$

where t_{mn} represents the mn^{th} element of the transmission/reflection matrix, and $A_n e^{j\phi_n}$ is the field from the n^{th} segment of the SLM used to perform the phase modulation. The source field is segmented by the SLM into N segments and reflected off the scattering medium. The field in the observation plane consists of a linear combination of these N segments of the source field at each of the M observation positions [5]. Normalizing Equation (1) to intensity, $A_n = \frac{1}{\sqrt{N}}$, and the observed intensity at the m^{th} position was given by Equation (2), also repeated here,

$$I_m = |E_m|^2 = \frac{1}{N}\left|\sum_{n=1}^{N} t_{mn} e^{j\phi_n}\right|^2 . \tag{2}$$

Intensity enhancement was defined by Vellekoop for transmissive inverse diffusion in Equation (3) as [7],

$$\eta = \frac{\langle I_{opt}\rangle}{\langle I_{rnd}\rangle}, \tag{3}$$

which is a simple ratio of the average intensity of the optimized spot divided by the average intensity of the unoptimized random speckle [6]. For transmission through a random medium, the t_{mn} terms follow a statistically independent complex circular Gaussian distribution [13] with properties that can be used to simplify Equation (3) and express the ideal intensity enhancement as a function of the total number of SLM segments [7], given in Equation (4) as,

$$\eta_{tranmissive} = \frac{\pi}{4}(N-1) + 1 \approx \frac{\pi}{4}N. \tag{4}$$

The multiple random paths light travels when transmitted through a scattering medium are not present in the reflection model. This lack of complex circular Gaussian statistics produces a different expression for ideal enhancement. Using a simplified geometric approximation, the surface properties are modeled as a constant average surface reflectivity and phase delay that is related to the reflector surface height fluctuations [10]. Using this model, Equation (2) is rewritten for the reflection case as

$$I_m = \frac{1}{N}\left|\sum_{n=1}^{N} \mathbf{r}\, e^{j\theta_{mn}} e^{j\phi_n}\right|^2 , \tag{5}$$

where $\mathbf{r}$ is the average surface reflectivity and θ_{mn} is the phase delay caused by the surface height fluctuations of the material. Rough surfaces have surface height

fluctuations spanning multiple wavelengths [10]. A rough surface modeled with a Gaussian surface height distribution with a standard deviation greater than half a wavelength, will produce a uniformly distributed phase when wrapped to the interval $[-\pi, \pi]$. Thus, the phase term of the reflector material, θ_{mn}, is assumed to have a uniform distribution over $[-\pi, \pi]$. The intensity achieves a maximum value when the SLM phase delay is set to cancel the phase delay imposed by the surface height of the reflector, $\phi_n = -\theta_{mn}$, for a given m, then

$$\langle I_{max} \rangle = \left\langle \frac{1}{N} \left| \sum_{n=1}^{N} \mathbf{r} \right|^2 \right\rangle = \mathbf{r}^2 N, \tag{6}$$

where the angled brackets, again, denote the ensemble average.

The unoptimized random speckle background can be expressed as a fixed-length random phasor sum,

$$\langle I_{rnd} \rangle = \left\langle \frac{1}{N} \left| \sum_{n=1}^{N} \mathbf{r}\, e^{j\theta_{mn}} \right|^2 \right\rangle = \mathbf{r}^2 \left\langle \left| \frac{1}{\sqrt{N}} \sum_{n=1}^{N} e^{j\theta_{mn}} \right|^2 \right\rangle, \tag{7}$$

which can be written as a complex number with amplitude A and phase Θ,

$$\langle I_{rnd} \rangle = \mathbf{r}^2 \left\langle \left| A e^{j\Theta} \right|^2 \right\rangle = \mathbf{r}^2 \left\langle A^2 \right\rangle, \tag{8}$$

where A and Θ are both random variables and $\langle A^2 \rangle$ is the second moment. The probability density function of A is given by [10],

$$p_A(\alpha) = 4\pi^2 A \int_0^\infty \rho J_0^N \left(\frac{2\pi\rho}{\sqrt{N}} \right) J_0(2\pi\alpha\rho) d\rho, \tag{9}$$

where $\alpha \geq 0$ is the magnitude of the random phasor sum, $\rho = \frac{\omega}{2\pi}$ from the 2-dimensional joint characteristic function of the random phasor sum [10], and J_0 is the zero-order Bessel function of the first kind. Using Equation (9), Mathematica® approximated the second moment, $\langle A^2 \rangle = 1$. Substituting the results from Equa-

tions (6) and (8) into Equation (3) shows the ideal enhancement for reflective inverse diffusion is equal to the total number of SLM segments N,

$$\eta_{reflective} = \frac{\langle I_{max} \rangle}{\langle I_{rnd} \rangle} = N. \tag{10}$$

3.2 Diffraction Theory

3.2.1 Rayleigh-Sommerfeld Diffraction.

The first Rayleigh-Sommerfeld diffraction formula can be seen as a mathematical representation of the Huygens-Fresnel principle. The formula shows that the field at an aperture of extent Σ, $U(P_1)$, can be described as an infinite number of point sources each producing its own spherical wave. The observed field, $U(P_0)$, is the sum of the contributions from these point sources. The integral form of the Rayleigh-Sommerfeld diffraction formula is given by,

$$U(P_0) = \frac{1}{j\lambda} \iint_{\Sigma} U(P_1) \, \frac{\exp(jkr_{01})}{r_{01}} \cos(\theta) \, \mathrm{d}s, \tag{11}$$

where λ is the optical wavelength, k is the propagation constant and equals $\frac{2\pi}{\lambda}$. The integration is over the enclosed surface S that contains P_1. The source and observation planes are separated by a screen that is opaque outside of the aperture represented by area Σ. The distance between the points in the source and observation planes is represented by r_{01}, and θ is the angle between the surface normal of the aperture and the ray to the observation point [35, 36].

Consider a system of two parallel planes, the source plane with coordinates (ξ, η), and the observation plane with coordinates (x, y). Since θ is the angle between the source plane's surface normal $(\hat{n})$ and the vector between P_0 and P_1 $(\vec{r}_{01})$, then $cos(\theta) = \frac{z}{r_{01}}$, where the z-axis and $\hat{n}$ are colinear. Thus, the field at any point in the

observation plane (x, y) can be thought of as a sum of contributions from an infinite number of point sources in the source plane where the limits of integration would depend on the aperture [35, 36].

$$U_2(x,y) = \frac{z}{j\lambda} \iint U_1(\xi,\eta)\, \frac{\exp(jkr_{01})}{r_{01}^2}\, \mathrm{d}\xi\, \mathrm{d}\eta \tag{12}$$

$$r_{01} = \sqrt{z^2 + (x-\xi)^2 + (y-\eta)^2} \tag{13}$$

Rayleigh-Sommerfeld diffraction requires only the distance between the points in the source and observation planes be much greater than the wavelength ($r_{01} \gg \lambda$). This is the most accurate scalar wave optics diffraction formula, and is the basis for Fresnel and Fraunhofer diffraction [36].

3.2.2 Fresnel Diffraction.

The square root in the distance term r_{01} in Equation (13), can cause problems with analytic solutions to diffraction. The square root can be eliminated by using the first two terms of its binomial expansion to approximate r_{01}.

$$\sqrt{1+b} = 1 + \frac{1}{2}b - \frac{1}{8}b^2 + ... \tag{14}$$

$$r_{01} = \sqrt{z^2 + (x-\xi)^2 + (y-\eta)^2} = z\sqrt{1 + \left(\frac{x-\xi}{z}\right)^2 + \left(\frac{y-\eta}{z}\right)^2} \tag{15}$$

$$r_{01} \approx z\left[1 + \frac{1}{2}\left(\frac{x-\xi}{z}\right)^2 + \frac{1}{2}\left(\frac{y-\eta}{z}\right)^2\right] \tag{16}$$

The r_{01} term appears in both the exponent and denominator of Equation (12). Since the denominator is a squared term, it is sufficient to reduce the approximation of

$r_{01} \approx z$. The r_{01} in the exponent is more susceptible to small changes, thus, Equation (16) is used [35], to produce

$$U_2(x,y) = \frac{z}{j\lambda} \iint U_1(\xi,\eta) \frac{\exp\left(jkz\left[1 + \frac{1}{2}\left(\frac{x-\xi}{z}\right)^2 + \frac{1}{2}\left(\frac{y-\eta}{z}\right)^2\right]\right)}{z^2} \,\mathrm{d}\xi\,\mathrm{d}\eta. \tag{17}$$

Now simplify by moving $\frac{e^{jkz}}{z^2}$ outside the integral to get

$$U_2(x,y) = \frac{e^{jkz}}{j\lambda z} \iint U_1(\xi,\eta) \exp\left(j\frac{k}{2z}\left[(x-\xi)^2 + (y-\eta)^2\right]\right) \mathrm{d}\xi\,\mathrm{d}\eta. \tag{18}$$

By expanding the quadratic in the exponential and moving $e^{j\frac{k}{2z}(x^2+y^2)}$ outside the integral, Equation (18) can be re-written as,

$$U_2(x,y) = \frac{e^{jkz}}{j\lambda z} e^{j\frac{k}{2z}(x^2+y^2)} \iint \left[U_1(\xi,\eta) e^{j\frac{k}{2z}(\xi^2+\eta^2)}\right] e^{-j\frac{2\pi}{\lambda z}(x\xi+y\eta)} \,\mathrm{d}\xi\,\mathrm{d}\eta. \tag{19}$$

Equation (19) is the Fresnel diffraction integral. The second exponential in the integral is the Fourier transform kernel. Given the approximation on r_{01}, this shows that the field in the observation plane is proportional to the two-dimensional Fourier transform of field in the source plane, $U_1(\xi,\eta)$, multiplied by a quadratic phase factor.

Determining the accuracy of the Fresnel integral is accomplished by looking at the approximation of r_{01}. The accepted condition for accuracy is when the $b^2/8$ term that was dropped from the r_{01} approximation causes a maximum phase change much less than 1 radian. The accuracy condition is met when the distance between the source and observation plane, z, satisfies Equation (20) [35],

$$z^3 \gg \frac{\pi}{4\lambda}[(x-\xi)^2 + (y-\eta)^2]^2_{max}. \tag{20}$$

As an example, for the propagation from the diffuse reflector to the CCD, the

diffraction-limited spot produced by the SLM and positive lens (L_1) represents the source aperture. The radius of the diffraction limited spot produced by the SLM and positive lens is given by [35],

$$q = \frac{\lambda f}{d_{seg}}, \tag{21}$$

where f is the focal length of the lens, and d_{seg} is the width of the SLM segment. For $N = 1,024$ SLM segments, then $d_{seg} = 240$ μm and the radius of the diffraction limited spot is approximately 1.3 mm. The dimension of the observation plane is the 6.9 mm by 4.3 mm of the CCD. The wavelength of the HeNe laser source used in the experiment is approximately 633 nm. Applying Equation (20) to the parameters of the original experiment, the Fresnel diffraction approximation would require a distance $z \gg 12$ cm. The observation plane is said to be in the near field when the z satisfies Equation (20).

3.2.3 Fraunhofer Diffraction.

Further assume that the distance between the source and observation plane is large enough that the quadratic exponent of the first exponential in Equation (19) can be approximated to be zero, so that

$$z \gg \frac{k(\xi^2 + \eta^2)_{max}}{2}. \tag{22}$$

Then, the Fresnel diffraction integral in Equation (19) can be re-written as the Fraunhofer diffraction integral,

$$U_2(x, y) = \frac{e^{jkz}}{j\lambda z} e^{j\frac{k}{2z}(x^2+y^2)} \iint U_1(\xi, \eta) e^{-j\frac{2\pi}{\lambda z}(x\xi+y\eta)} \, \mathrm{d}\xi \, \mathrm{d}\eta. \tag{23}$$

The distance requirement imposed by Equation (22) can be very large. Due to the

large distances required for Fraunhofer diffraction, it is commonly referred to as the far field approximation [36]. Using the original experimental parameters, the radius of the diffraction limit spot is 1.3 mm as the source aperture with a HeNe laser wavelength of 633 nm; Equation (22) requires a distance of $z \gg 17$ m for Fraunhofer diffraction approximation to be valid.

It is possible to reduce the distance requirement of Equation (22) by the use of a positive lens. The positive lens of focal length f, imparts a quadratic phase, given by Equation (24), onto the source field directly in front of the lens,

$$t_A(\xi, \eta) = \exp\left[-j\frac{k}{2f}(\xi^2 + \eta^2)\right]. \tag{24}$$

The total source field is then given by

$$U_0(\xi, \eta) = U_1(\xi, \eta)\ P(\xi, \eta)\ t_A(\xi, \eta), \tag{25}$$

$$P(\xi, \eta) = \begin{cases} 1, & \text{inside the lens aperature.} \\ 0, & \text{otherwise.} \end{cases} \tag{26}$$

where $P(\xi, \eta)$ is the pupil function of the lens aperture. Substituting Equation (25) into the Fresnel diffraction integral in the Equation (19) gives,

$$U_2(x, y) = \frac{e^{jkz}}{j\lambda z} e^{j\frac{k}{2z}(x^2+y^2)} \iint U_1(\xi, \eta)\ P(\xi, \eta)\ t_A(\xi, \eta) e^{j\frac{k}{2z}(\xi^2+\eta^2)} e^{-j\frac{2\pi}{\lambda z}(x\xi+y\eta)}\, \mathrm{d}\xi\, \mathrm{d}\eta \tag{27}$$

where the quadratic phase imparted by the lens cancels out the quadratic phase in the Fresnel diffraction integral when $z = f$. This leaves only the Fourier transform of the source field and pupil function product. If the extent of the lens pupil function

P is much larger than that of the source field U_1, then the effect of the lens aperture can be neglected leaving only the source field,

$$U_2(x,y) = \frac{e^{jkf}}{j\lambda f} e^{j\frac{k}{2f}(x^2+y^2)} \iint U_1(\xi,\eta)\, e^{-j\frac{2\pi}{\lambda f}(x\xi+y\eta)}\, \mathrm{d}\xi\, \mathrm{d}\eta. \tag{28}$$

Equations (28) and (23) are identical for $z = f$, but Equation (28) did not require use the stringent requirements on z of Equation (22) [35].

The Fresnel number provides a more straight forward method to determine when it is appropriate to apply either the Fresnel or Fraunhofer approximation to diffraction. Let w represent the half width of the aperture, the Fresnel number (N_F) is then given by

$$N_F = \frac{w^2}{\lambda z}. \tag{29}$$

For a Fresnel number approximately equal to one ($N_F \approx 1$), it is common to apply Fresnel Diffraction. In some cases, Fresnel diffraction may be reasonably accurate for Fresnel numbers as high as 30. The Fresnel number for Fraunhofer diffraction can be determined from Equations (22) and (29),

$$\begin{aligned} z &\gg \frac{k(\xi^2+\eta^2)_{max}}{2} = \frac{\pi w^2}{\lambda} \\ 1 &\gg \frac{\pi w^2}{\lambda z} = \pi N_F. \end{aligned} \tag{30}$$

The factor of π is often dropped and the Fresnel number for Fraunhofer diffraction is accepted as simply much less than one ($N_F \ll 1$). Outside these regions Rayleigh-Sommerfeld diffraction should be used to maintain accuracy [36].

3.2.4 Transfer Functions.

Diffraction integrals can become very complex, very quickly. A different approach is to treat the field propagation through the system as a linear spatial filter. The impulse response of Rayleigh-Sommerfeld diffraction is given by [35],

$$h(x,y) = \frac{z}{j\lambda}\frac{\exp(jkr)}{r^2}, \tag{31}$$

where z is the propagation distance, λ is the wavelength, the wavenumber is $k = \frac{2\pi}{\lambda}$, and $r = \sqrt{z^2 + x^2 + y^2}$. The impulse response can be used to rewrite the Rayleigh-Sommerfeld diffraction integral in Equation (12) as a convolution,

$$U_{out}(x,y) = \frac{z}{j\lambda}\iint U_{in}(\xi,\eta)\, h(x-\xi, y-\eta)\, \mathrm{d}\xi\mathrm{d}\eta. \tag{32}$$

Applying the Fourier transform convolution theorem, Equation (32) can be rewritten as,

$$\begin{aligned} U_{out}(x,y) &= \frac{z}{j\lambda}\,\mathcal{F}^{-1}\{\mathcal{F}\{U_{in}(\xi,\eta)\}\,\mathcal{F}\{h(x,y)\}\} \\ &= \frac{z}{j\lambda}\,\mathcal{F}^{-1}\{\mathcal{F}\{U_{in}(\xi,\eta)\}\,H(f_x,f_y)\} \end{aligned} \tag{33}$$

where the transfer function, $H(f_x, f_y)$, is the Fourier transform of the impulse response $h(x,y)$ [35].

3.3 Mathematical Model

Scalar diffraction theory was used to develop a mathematical description of reflective inverse diffusion. The propagation distance of 50 cm from the diffuse reflector to the CCD is greater than the near-field distance of 12 cm calculated in Section 3.2.2

using Equation (20). Whether this satisfies the much greater than requirement of Equation (20) is open for interpretation. However, since the number of operations is identical in MATLAB® regardless of which transfer function is used, the more accurate Rayleigh-Sommerfeld diffraction formula is used for propagation. The transfer function for Rayleigh-Sommerfeld diffraction is [35],

$$H(f_x, f_y) = \exp\left(jkz\sqrt{1-(\lambda f_x)^2-(\lambda f_y)^2}\right), \tag{34}$$

where z is the propagation distance, λ is the optical wavelength, k is the wavenumber $2\pi/\lambda$, and f_x and f_y are the respective horizontal and vertical spatial frequencies of the source field. Using the transfer function to propagate the source field $U_{src}(x, y)$ a distance z, the observed field is given by [36]

$$U_{obs}(x, y) = \frac{z}{j\lambda}\,\mathcal{F}^{-1}\{\mathcal{F}\{U_{src}(x, y)\}\,H(f_x, f_y)\}, \tag{35}$$

where (x, y) are the Cartesian coordinates orthogonal to z-direction corresponding to the spatial frequencies (f_x, f_y).

The field at each pixel of the SLM when illuminated by a plane wave can be considered simply as the phase delay applied at that pixel. Using Equation (35), the field is propagated from the SLM to just prior to lens L_1 in Figure 2, normalized with constant phase terms removed is

$$U_{L_1}^{-}(x, y) = \mathcal{F}^{-1}\{\mathcal{F}\{U_{SLM}(x, y)\}\,H(f_x, f_y)|_{z=Z_1}\}, \tag{36}$$

where Z_1 is the distance from the SLM to lens L_1. The Fourier transform property of lens L_1 is then used to determine the field at the diffusely reflecting sample located at the lens focus,

$$
\begin{aligned}
U^{-}_{sample}(x,y) &= e^{j\frac{k}{2f}(u^2+v^2)}\mathcal{F}\{U^{-}_{lens}(x,y)\} \\
&= e^{j\frac{k}{2f}(u^2+v^2)}\mathcal{F}\{\ \mathcal{F}^{-1}\{\mathcal{F}\{U_{SLM}(x,y)\}\ H(f_x,f_y)|_{z=Z_1}\}\} \\
&= e^{j\frac{k}{2f}(u^2+v^2)}\mathcal{F}\{U_{SLM}(x,y)\}\ H(f_x,f_y)|_{z=Z_1}.
\end{aligned}
\tag{37}
$$

Lens L_1 causes a coordinate transformation to the (u,v) plane which is related to the spatial frequencies by $u = \frac{\lambda f_x}{z}$ and $v = \frac{\lambda f_y}{z}$, where $z = Z_1$ [35].

The field at the sample given by Equation (36) is multiplied by $e^{j\theta(u,v)}$ which represents the phase scattering properties of the reflector. The result is then propogated to the CCD detector in the observation plane using Equation (35),

$$
\begin{aligned}
&U_{CCD}(u,v) = \\
&\qquad \mathcal{F}^{-1}\{\mathcal{F}\{e^{j\frac{k}{2f}(u^2+v^2)}e^{j\theta(u,v)}\mathcal{F}\{U_{SLM}(x,y)\}H(f_x,f_y)|_{z=Z_1}\}\ H(f_u,f_v)|_{z=Z_2}\},
\end{aligned}
\tag{38}
$$

where (x,y) are the coordinate axes of the SLM and (f_x,f_y) are the respective horizontal and vertical spatial frequencies of the field at the SLM. The coordinate axes of the reflective sample are (u,v), and (f_u,f_v) are the respective horizontal and vertical spatial frequencies of the field at the reflector. The focal length of lens L_1 is f, and Z_1 and Z_2 are the distances from the SLM to the lens and from the reflective sample to the CCD, respectively. This transform relationship is unique to the reflective inverse diffusion setup in Figure 2. Transmissive inverse diffusion uses microscope objectives on both sides of the scattering sample that beam-contracts the light from the SLM onto the sample and then re-images the light leaving the sample onto the CCD (see Figure 2 in reference [6]). The differences in the experimental setups create different transform relationships for reflective and transmissive inverse diffusion. However, since both processes are linear, Equation (1) is valid for both.

3.4 Sample Plane Pixel Size

The sample spacing of the simulated SLM was fixed at 15 μm to match the pixel spacing of the physical SLM. The pixel spacing establishes the maximum spatial frequency of $[f_\xi]_{max} = \frac{1}{2\Delta\xi} = 33.3\frac{cycles}{mm}$. The result for $[f_\eta]_{max}$ is identical since the pixel spacing is uniform both vertically and horizontally. The spatial frequency step size is $\Delta f_\xi = \frac{1}{L_\xi}$, where L_ξ is the length of the source plane in the ξ-direction. Since the source plane is square, $L_\xi = L_\eta = L_1$, and $\Delta f_\xi = \Delta f_\eta$. The size L_1 must at a minimum be equal to the dimension of the SLM, 7.68 mm; however it is often recommended that L_1 be two or three times this size [36]. Using the values of $[f_\xi]_{max}$ and Δf_ξ, the range of spatial frequencies is given by,

$$f_\xi \rightarrow \left[-\frac{1}{2\Delta\xi} : \frac{1}{L_1} : \frac{1}{2\Delta\xi} - \frac{1}{L_1}\right], \tag{39}$$

with a similar result for f_η. Thus, the spatial frequency resolution can be increased by increasing L_1. This is accomplished by padding the simulated SLM input with zeros.

The spacing at the diffuse reflector is then $\Delta x = \frac{\lambda f}{L_1}$. It is possible to pad L_1 large enough to achieve wavelength-scale values for Δx in an attempt to simulate the sampling the imperfections of the reflector surface. This, however, should be avoided as scalar diffraction theory would no longer be a valid approximation, and the increase in the size of L_1 causes a substantial increase in processing time.

3.5 Simulations

A diffraction-based propagation model allowed for examination of the field at any point in the simulation. Using MATLAB® to calculate the field at the CCD using Equation (38), an Intel Core i7® computer with 8 gigabytes of RAM could

complete over 2 optimizations per second, which was more that 64 times faster than experimental methods with available equipment. The MATLAB® source code for the simulations can be found in Appendix A. This model was validated using a mirror as a test case.

The diffusely reflecting sample was replaced by a mirror to validate the propagation-based simulation. In simulation, the mirror is considered a perfect reflector, which eliminates the $e^{j\theta(x,y)}$ term from Equation (38). Qualitatively, with a mirror positioned at the focus of the positive lens, the creation of a focused spot on the CCD simply requires shifting the focus of the positive lens the distance from the mirror to the CCD. This is accomplished by applying a negative lens phase screen to the SLM. The phase screen for a lens was given in Equation (24). Using geometric optics, the focus of the negative lens is given by,

$$f_{SLM} = \frac{1}{\frac{1}{f} - \frac{1}{f+Z_2}} - Z_1, \tag{40}$$

where Z_1 is the distance from the SLM to the positive lens, f is the focal length of the positive lens, and Z_2 is the distance from the mirror to the CCD.

The spot produced by the mirror test case was captured by the CCD and compared with the spot simulated using Equation (38). Figure 5 shows both the measured and simulated spots and includes the center horizontal cross sections of each. There was a 20-μm difference between the FWHM diameter of the measured and simulated spots. The difference is attributed to uncertainties in the experimental distances between the SLM, lens, reflector, and CCD that result a small defocus error in the measured spot.

Computer simulations of the original reflective inverse diffusion experiments corroborate the experimental data. The experimental enhancement is plotted per iteration of the algorithm in Figure 6(a). The effects of speckle decorrelation were

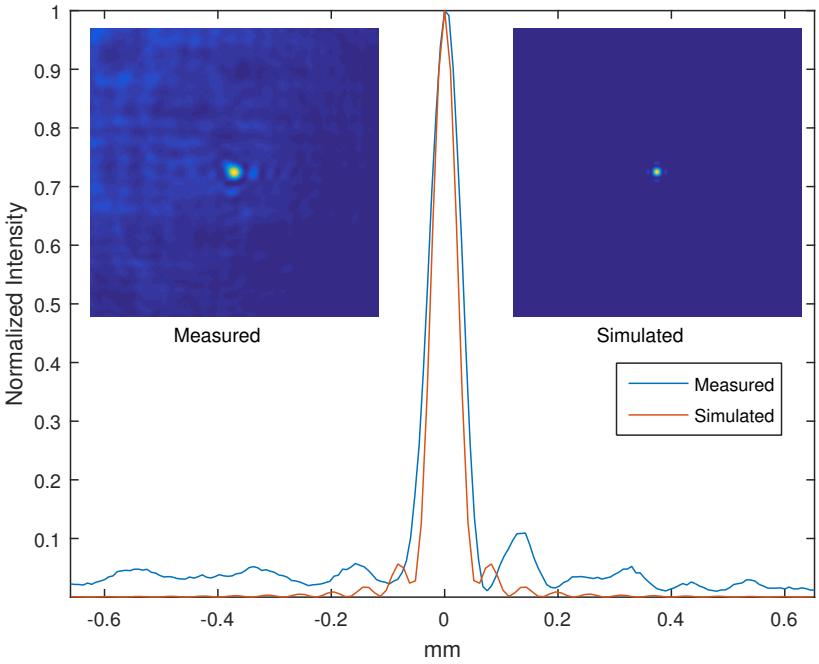

Figure 5. Simulation Validation. The diffusely reflecting sample was replaced by a mirror to compare measured and simulated intensity patterns. A negative lens phase screen was used to position the focus onto the CCD.

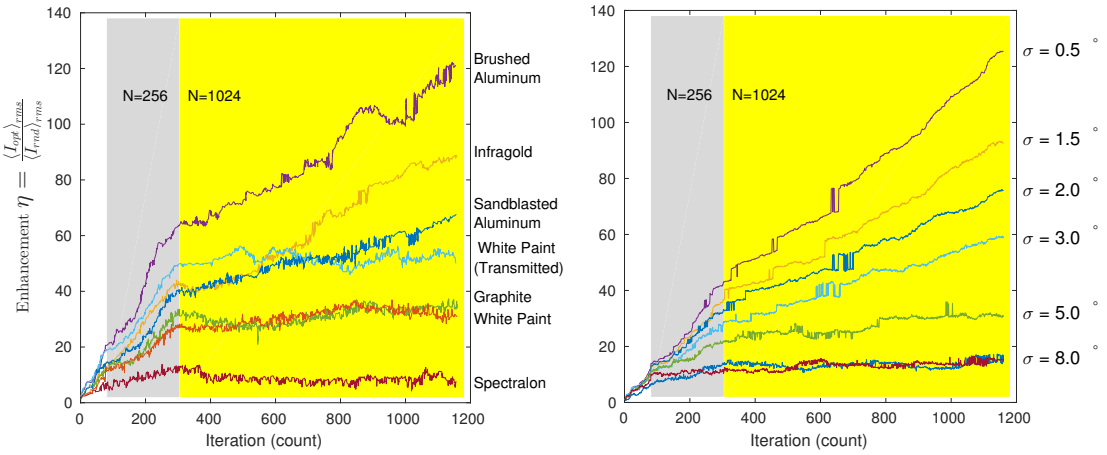

Figure 6. Enhancement performance comparison of simulated and experimental data. The N=256 iterations are highlighted in gray. The N=1,024 iterations are highlighted in yellow. (a) Enhancement achieved in laboratory experiments for each of the six reflector materials. Reprinted with permission [9]. (b) Enhancement achieved in simulations of reflective inverse diffusion with zero-mean Gaussian distributed random phase fluctuations added to the reflector model. With the exception of $\sigma = 8°$, all reflector models are unimodular with a uniformly distributed random phase. For $\sigma = 8°$, both the uniformly distributed random phase model (red) and the circular Gaussian model (blue) are shown.

simulated by adding a zero-mean random Gaussian-distributed phase to the reflector model each time the intensity was calculated. The standard deviation (σ) of the random phase fluctuation was dependent on the severity of decorrelation time of the material. Brushed aluminum maintained the highest correlation coefficient over time, thus experienced the lowest amount of enhancement loss attributed to speckle decorrelation. Simulations of the metal samples corresponded to a Gaussian phase fluctuation with standard deviation of 0.5° to 2°. The more diffuse samples, such as graphite and white paint, matched with a standard deviation of 3° to 5°. Figure 6(b) shows enhancement per iteration for a given standard deviation of the Gaussian phase fluctuation.

Spectralon® is a bulk scatter, and due to a high depth of light penetration, was considered similar to the random paths experienced by light when transmitted through a scattering medium. Simulations of both the circular Gaussian model from transmissive inverse diffusion and uniform phase model produced similar enhancement with the same phase fluctuation standard deviation deviation of $\sigma = 8°$ (see Figure 6(b)). The enhancement for the uniform phase model does initially rise faster than the circular Gaussian model, which is expected based on the slopes of Equations (4) and (10). However, due to the decorrelation effects and limited number of phase values used in the optimization process, neither model was significantly better than the other at simulating the Spectralon® results.

3.6 Observation

The iterative algorithm of reflective inverse diffusion is a simple brute force method for determining phase screens that refocus light after reflection, but it also has several drawbacks. Only a small number of phase values can been tested, and each additional phase value that is added requires an additional N intensity measurements. Each time

the target segment in the observation plane changes locations, the entire algorithm must be completely restarted. The reflection matrix method discussed in the Chapter IV can solve both of these issues by measuring the phase contributions of the reflector.

IV. Reflection Matrices

4.1 Introduction

Dual photography is a method for mathematically interchanging the positions of a camera and light source. This is accomplished by taking advantage of Helmholtz reciprocity. A pixelated light source is used to illuminate a scene while a camera, with a different viewpoint than the light source, records images of light reflection and scattering from the target scene. These images are used to construct a transport matrix that maps light source pixels to camera pixels. The transport matrix is used to construct an image of the scene from the perspective of the light source. The reconstructed image contains information that was not directly visible from the perspective of the camera [2].

Target scene information hidden from the camera but recovered using dual photography must be visible from the perspective of the light source. This requirement limits the usefulness outside the author's original work of relighting scenes. Indirect photography is a method, developed at the AFIT, that sought to co-locate the light source with the camera, by eliminating the line-of-sight requirement of the light source, while maintaining the ability to reconstruct images not directly visible from the camera. The initial experiments using multiple reflection radiometric models achieved limited success [3, 4].

The basis for imaging with light scattered by transmission through, or reflect off, an object was established by Freund. The random scatterer was treated as a complex field that interfered with incident light to produce a distinct speckle pattern. It was theorized that by properly modifying the incident light, the scatterer could be used to simulate various optical instruments such as a lens or a mirror [37]. In the case of the mirror, this would allow the imaging of objects using diffusely reflected light from

a wall and to effectively see around corners. Proper development of these methods could have profound impact in remote sensing and other fields.

Phase modulation techniques have demonstrated the ability to shape a wavefront, causing light to refocus to a single point after transmission through a scattering medium. This process, called "inverse diffusion" by the authors, was also capable of controlling the location of the focused spot in the observation plane by adjusting the wavefront shape. The scattering of light is a linear process, whether caused by transmission through a medium or reflection off its surface [6,7]. Applying the concept of inverse diffusion to indirect photography, refocusing light from the first diffuse reflection has the potential to simplify the method back to that of dual photography. From the observation plane perspective, the origin of the light source is the first diffuse reflector, thus satisfying the line of sight requirement of dual photography. It has been demonstrated that the iterative techniques for wavefront shaping developed by Vellekoop *et al.* can be adapted to work in reflection [38].

Matrix methods for inverse diffusion have been developed with significant advantages over iterative techniques for refocusing light after transmission through a turbid medium [14,15,17,19,21,23]. The number of required intensity measurements are significantly reduced compared to iterative methods and the phase information collected allows refocusing of the light to any location in the observation plane, including producing multiple foci simultaneously. Adapting these methods for reflection would potentially bridge the gap between dual photography and indirect photography allowing images to be produced from reflectively scattered light and see around corners.

4.2 Methodology

4.2.1 Parallel Wavefront Optimization.

The method used to measure the RM was based on work by Yoon *et al.* for measuring transmission matrices of turbid media [17]. Yoon's method was based on parallel wavefront optimization method by Cui and expanded to measure the entire transmission matrix, rather than optimize to a single point [17, 19]. Parallel wavefront optimization uses interference between reference and signal fields produced by the SLM to extract the phase information of the RM [17,19]. The reference field is generated by static segments of the SLM and the signal field generated by modulated segments of the SLM.

The SLM is divided into N segments and the segments are separated into two interleaved groups. Each segment of Group 1 is modulated at a distinct frequency, while all the segments in Group 2 are held static as shown in Figure 7(a) (similar to Figure 2 from reference [17], modified for clarity). However, assuming the SLM is illuminated with a plane wave and all the segments are initially set to zero phase delay, using Equation (1), the field at the m^{th} position becomes,

$$E_m = \sum_{n=G+1}^{N} t_{mn} + \sum_{p=1}^{G} t_{mp} e^{j\omega_p t}, \tag{41}$$

where G is the total number of segments in Group 1, and $\phi_p = \omega_p t$ is the phase value of the SLM segments at time t. The first summation in Equation (41) represents the static reference field produced by the segments in Group 2 and simplifies to a complex number that will be represented by R_{m2}. The intensity at the m^{th} position is then given by,

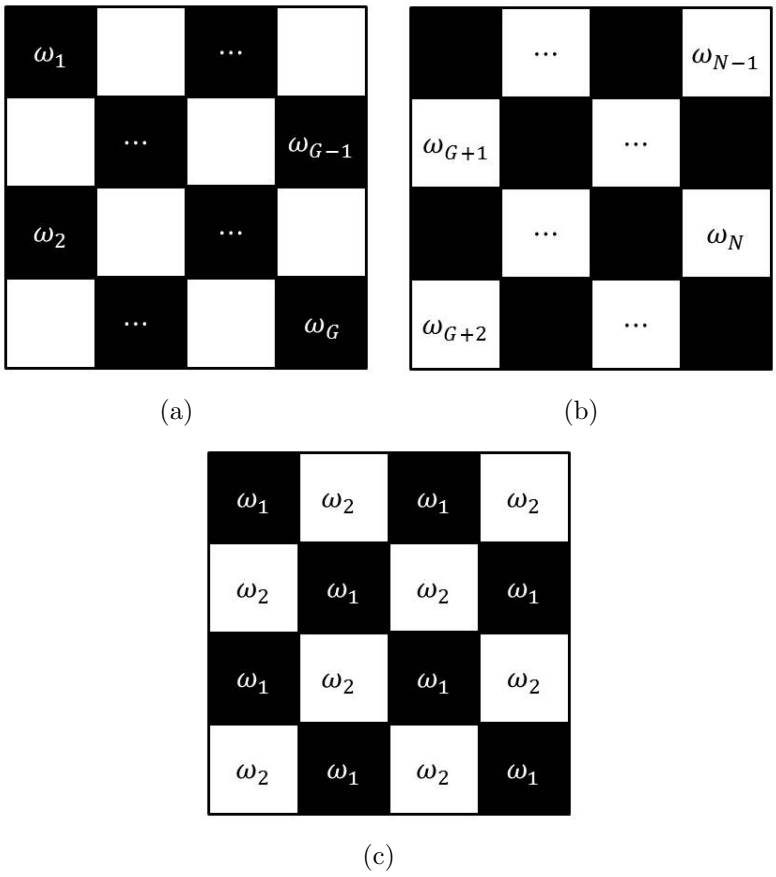

Figure 7. SLM segment diagram for parallel wavefront optimization. (a) Group 1 segments (black) are modulated, each at a distinct frequency, while Group 2 segements (white) are static. (b) Group 2 segments (white) are modulated, each at a distinct frequency, while Group 1 segments (black) are static. (c) All Group 1 segments (black) are modulated at ω_1, while all Group 2 segments (white) are modulated at ω_2 (similar to Figure 2 from reference [17], modified for clarity).

$$
\begin{aligned}
I_m = |E_m|^2 &= \left| R_{m2} + \sum_{p=1}^{G} t_{mp} e^{j\omega_p t} \right|^2 \\
&= |R_{m2}|^2 + R_{m2}^* \sum_{p=1}^{G} t_{mp} e^{j\omega_p t} + R_{m2} \sum_{p=1}^{G} t_{mp}^* e^{-j\omega_p t} + \sum_{p=1}^{G} \sum_{q=1}^{G} t_{mp}^* t_{mq} e^{j(\omega_q - \omega_p)t}.
\end{aligned} \tag{42}
$$

The desired matrix information is contained in the second term of Equation (42). Since the desired information occurs at specific frequencies, the $R_{m2}^* t_{mp}$ coefficients can be determined using the Fourier transform of the intensity measurements [17].

The frequencies for the modulated SLM segments are given by,

$$
\omega_p = \frac{G + p}{4G} \omega_s, \tag{43}
$$

where ω_s is the sampling frequency. This ensures that $\omega_p \in (\frac{1}{4}\omega_s, \frac{1}{2}\omega_s]$ and the harmonic frequencies $(\omega_q - \omega_p) \in [-\frac{1}{4}\omega_s, \frac{1}{4}\omega_s]$ do not overlap [17]. This requires $4G$ intensity measurements for proper resolution in the frequency domain in order to extract all the $R_{m2}^* t_{mp}$ terms. The roles of the SLM segment groups are then reversed, Group 1 segments are held static while Group 2 segments are modulated as shown in Figure 7(b). An additional $4(N - G)$ intensity measurements are recorded making the total number of intensity measurements $4N$ [17]. Fourier transforms are used to extract the $R_{m1}^* t_{mp}$ terms from the second set of intensity measurements. This results in an $M \times N$ matrix of $R_{mx}^* t_{mp}$ values that contains the phase information relating each segment of the SLM to each segment of the CCD detector. The matrix coefficients are simply amplitude scaling and phase shifts to provide the proper linear combination of the fields from the SLM segments that produces the field at the CCD in the observation plane. Thus, the coefficients are by definition unitless.

4.2.2 Reference Field Phase Matching.

The matrix of values collected consists of $R^*_{m2}t_{mp}$ terms from the optimization of Group 1 segments and $R^*_{m1}t_{mp}$ terms from the optimization of Group 2 segments. There is also an ambient static reference field, R_{m0}, produced by real world device and laboratory imperfections. Thus, the matrix values can be represented by [17],

$$\begin{aligned} &Group\ 1 : (R_{m0} + R_{m2})^*(t_{m1}, t_{m2}, \cdots, t_{mG}) \\ &Group\ 2 : (R_{m0} + R_{m1})^*(t_{m(G+1)}, t_{m(G+2)}, \cdots, t_{mN}). \end{aligned} \tag{44}$$

The different reference fields provide a different amplitude scaling and phase shift to the two SLM segment groups. Since the SLM is a phase-only device, the different amplitude scaling is of little concern. However, the phase difference between the two reference fields must be determined in order to build the final RM.

The phase shift between the two reference fields can be determined by modulating both SLM segment groups at different frequencies. This is similar to the previous step, except all the SLM segments of a given group are modulated at the same frequency as shown in Figure 7(c). The two frequencies used for this part of the process can be determined using Equation (43) with $G = 2$. The field produced at the CCD is then a sum of the ambient field, R_{m0}, and the modulated reference fields R_{m1} and R_{m2}. The equation for intensity becomes [17],

$$\begin{aligned} I_m = |E_m|^2 &= \left|R_{m0} + R_{m1}e^{j\omega_1 t} + R_{m2}e^{j\omega_2 t}\right|^2 \\ &= \sum_{k=0}^{2} |R_{mk}|^2 + R_{m0}R^*_{m1}e^{-j\omega_1 t} + R_{m0}R^*_{m2}e^{-j\omega_2 t} + R_{m1}R^*_{m2}e^{-j(\omega_2-\omega_1)t} \\ &\quad + R^*_{m0}R_{m1}e^{j\omega_1 t} + R^*_{m0}R_{m2}e^{j\omega_2 t} + R^*_{m1}R_{m2}e^{j(\omega_2-\omega_1)t}. \end{aligned} \tag{45}$$

Fourier transforms are used to extract the reference field coefficients from Equation (45). Eight intensity measurements are required for proper frequency domain resolution. These coefficients are used to determine the phase shift necessary to bring the optimized Group 2 SLM segments in phase with the optimized Group 1 SLM segments. The phase shift for the optimized Group 2 SLM segments is given by [17],

$$\begin{aligned} C &= (R_{m0} + R_{m2})^* (R_{m0} + R_{m1}) = |R_{m0}|^2 + R_{m0}^* R_{m1} + R_{m0} R_{m2}^* + R_{m1} R_{m2}^* \\ &= \frac{(R_{m0} R_{m2}^*)(R_{m0}^* R_{m1})}{R_{m1} R_{m2}^*} + R_{m0}^* R_{m1} + R_{m0} R_{m2}^* + R_{m1} R_{m2}^* \end{aligned} \tag{46}$$

Using the coefficients extracted from Equation (45), the phase shift term $\frac{C}{|C|}$ is calculated and applied to the optimized Group 2 SLM segments.

$$\begin{aligned} Group\ 1 &: \frac{|R_{m0} + R_{m2}|}{|R_{m0} + R_{m2}|} (R_{m0} + R_{m2})^* (t_{m1}, t_{m2}, \cdots, t_{mG}) \\ Group\ 2 &: \frac{|R_{m0} + R_{m1}|}{|R_{m0} + R_{m2}|} (R_{m0} + R_{m2})^* (t_{m(G+1)}, t_{m(G+2)}, \cdots, t_{mN}). \end{aligned} \tag{47}$$

The term $\frac{(R_{m0}+R_{m2})^*}{|R_{m0}+R_{m2}|}$ is now common to both groups. This phase only term shows that the reference field phase contribution to the RM is simply a global phase shift and can be ignored [17]. The RM values are

$$\begin{aligned} Group\ 1 &: |R_{m0} + R_{m2}| (t_{m1}, t_{m2}, \cdots, t_{mG}) \\ Group\ 2 &: |R_{m0} + R_{m1}| (t_{m(G+1)}, t_{m(G+2)}, \cdots, t_{mN}), \end{aligned} \tag{48}$$

which shows the reference fields for the two optimized groups still have different amplitude scalings, but since the SLM is phase modulation only, this difference is ignored. The argument of Equation (48) provides the phase information for the

RM [17].

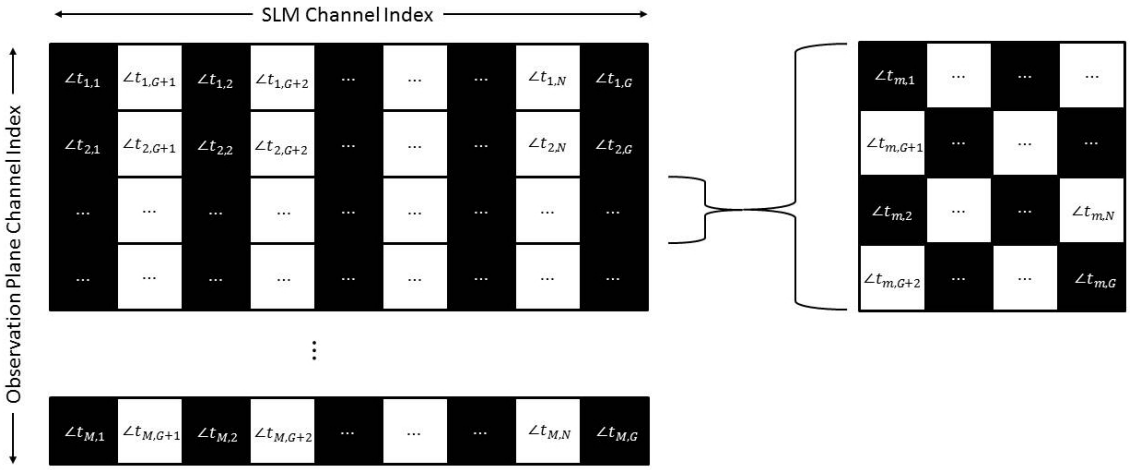

Figure 8. The RM has dimensions $M \times N$ and contains the phase information of the light at each CCD channel from each SLM channel. To refocus the light to a specific CCD channel the corresponding row of the RM values is conjugated to bring all the incident light on that CCD channel in to phase. The conjugate RM row vector is reshaped according to the dimensions of the SLM and applied.

The RM is constructed from Equation (48) as show in Figure 8. This matrix describes the effect the scattering sample has on the phase of the incident light from every SLM channel to every observation plane channel. To focus light into a specific channel, extract the row corresponding to the desired observation plane channel and reshape the row vector to a matrix corresponding to the SLM pixels (as shown in Figure 8). These phase values are then conjugated and applied to the SLM [17].

The RM is capable of generating multiple foci simultaneously. This is done by a linear combination of phases from multiple rows of the reflection matrix. The phase values applied to the SLM are given by,

$$SLM_{foci} = \sum_{m=1}^{K} \frac{1}{\sqrt{K}} \left(\angle t_{mp}\right)^{\dagger}, \tag{49}$$

where † indicates the complex conjugate, and $\angle t_{mp}$ is the argument of the complex value t_{mp}. Thus, the phase applied to each SLM segment is an average of the values

from the RM for the individual observation plane channels. Different foci can be given different weights by replacing the $\frac{1}{\sqrt{K}}$ with α_m, where $\sum \alpha_m^2 = 1$. The SLM phase map for multiple foci with different scaling factors is then [17],

$$SLM_{foci} = \sum_{m=1}^{K} \alpha_m \left(\angle t_{mp}\right)^{\dagger}. \tag{50}$$

Since magnitude information of the RM is not available, and only phase modulation is used to refocus light, different observation plane channels will experience different levels of enhancement. Equation (50) provides a method of controlling the relative enhancement of each of the targeted observation plane channels [17].

4.2.3 Simulation Setup.

Simulations were conducted in MATLAB® using Equation (38) to determine the field and intensity in the observation plane. The MATLAB® source code is available in Appendix A. The distances Z_1 and Z_2 from Figure 2 are 15 cm and 50 cm respectively and the lens focus is $f = 500$ mm. A single SLM pixel is 15 μm square and is represented by a single pixel in the simulation. The 512 by 512 array of SLM values is then zero-padded to provide the "guard-area" for diffraction to prevent artifacts at the edges of the simulated SLM [36]. Due to the spatial Fourier transform produced by the positive lens, the amount of zero-padding directly affects the spatial frequency resolution which determines the pixel size in the observation plane. The pixel size in the observation plane is given by,

$$\Delta x_{obs} = \frac{\lambda f}{L} \tag{51}$$

where L is the length of the zero-padded SLM. For all simulations, 256 zeros where padded to all sides of the simulated SLM for a total of 1024×1024 pixels, each 15-μm

square for a total area of 15.36 mm square. This established the observation plane pixel size at 20.6 μm. The pixel size in the observation plane is of particular significance because the observation-plane and sample-plane spacings are the same. Thus, the pixel size in the observation plane represents the minimum lateral correlation length of the simulated scattering sample.

4.2.4 Experimental Setup.

The experimental setup was shown in Figure 2. A Thorlabs 5-mW HeNe laser ($\lambda = 632.8$ nm) with a linearly polarized output is used as the illumination source. The Meadowlark P512 is a reflective SLM that is 7.68 mm by 7.68 mm, consisting of 512 by 512 pixels, each capable of over 16,000 discrete phase levels over a 2π phase stroke. Feedback is provided by a Thorlabs 4070-GE CCD with 2048 by 2048 pixels and a pixel pitch of 7.5 μm by 7.5 μm.

The laser is first expanded and collimated to fill the SLM. A non-polarizing beam splitter (NPBS) is used to maintain normal incidence with the SLM. The distance Z_1, from the SLM to lens L_1 is 15 ± 0.5 cm. After modulation, the beam is focused by a 500-mm lens, L_1, onto the scattering sample placed at the lens focus. The sample is a 6-inch square of polished aluminum. The CCD was placed 50 ± 0.5 cm from the scattering sample. Both SLM and CCD are controlled through MATLAB®. The RM values are determined using MATLAB® fast Fourier transform (FFT) of the intensity measurements from the CCD.

4.3 Results and Analysis

4.3.1 Simulation Results.

The simulated speckle patterns did not extend across the entire 1024 by 1024 pixel area of the observation plane. Since these simulations involve large arrays of

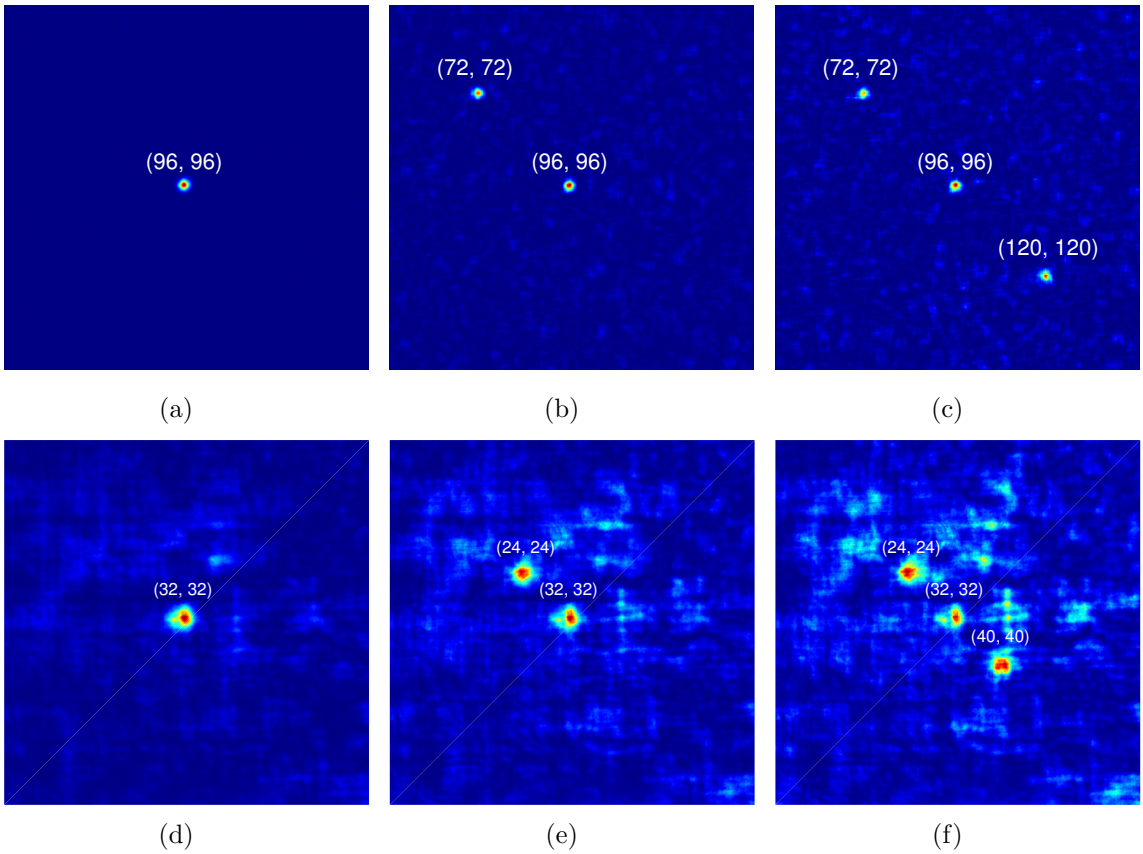

Figure 9. Observation plane intensity patterns (a)-(c) are computer simulations and (d)-(e) are laboratory results of the focal-plane system in Figure 2 with the polished almuninum sample. Above each spot are the (row, column) coordinates of the given observation plane segment. Phase maps generated by the RM are used to refocus light to single or multiple segments in the observation plane. (a) A simulated single-segment enhancement of $\eta = 348$ over background speckle. (b) Simulation of two foci optimized simultaneously at $(72, 72)$ and $(96, 96)$ with enhancements of $\eta = 47$ and 56, respectively. (c) Simulation of three foci generated with increased background speckle at $(72, 72)$, $(96, 96)$, and $(120, 120)$ with enhancement values of $\eta = 26$, 32, and 29, respectively. (d) Demonstrated single-segment enhancement of $\eta = 18$ over background speckle. (e) Two segments are optimized simultaneously, measured enhancement for both foci is $\eta = 10$. (f) Three foci are generated with increased background speckle at $(24, 24)$, $(32, 32)$, and $(40, 40)$, enhancement values are $\eta = 7$, 6, and 7, respectively.

data, only the center 768 by 768 pixels of the observation plane, where the speckle patterns are the strongest, were used for determining the RM. To further reduce the computer memory requirements of the simulations, the windowed observation plane measurements were binned into M channels. Ideal enhancement is given in Equation (10) and depends on N, the total number of SLM segments. The simulations show a relationship to M; in general, larger values for M increase the enhancement of the spot the RM is able to produce. Since the total number of intensity measurements is $(4N + 8)$, any increase in N increases the runtime by a factor of 4. However, increasing M only increases the amount of computer memory required.

It was observed that if M was of insufficient size, then the reference field phase matching procedure described in section 4.2.2 failed to increase enhancement of the spot produced by the RM. Smaller M values produce larger individual channels. This allows for Group 1 and Group 2 SLM pixels to optimize to different locations within the larger observation plane channel and produce a larger blurred-out spot with lower overall enhancement. Segmenting the 768 by 768 pixels of the observation plane into $M = 36,864$ channels provided the necessary resolution such that the reference field phase matching process significantly improved spot enhancement produced by the RM. The $M = 36,864$ channels are arranged 192 by 192 over the observation plane. Each channel consists of 4 by 4 pixels that represents a simulated area of 82.4 μm square.

The RM was used to refocus the incident beam to 1,024 of the 36,864 observation plane channels. The selected channels were evenly spaced throughout the observation plane. The average enhancement of the sampled channels was $\eta_{avg} = 307$ with a maximum enhancement of $\eta_{max} = 398$. This represents roughly 30%-40% of the maximum ideal enhancement of Equation (10). Simulation time was approximately 300 seconds on an Intel® i7 desktop computer with 8 gigabytes of memory. Each

value of m has a (row, column) coordinate corresponding to its location in the 192 by 192 channel array representing the observation plane. The simulated RM was used to optimize the intensity at center channel $(96, 96)$, m=18,336. This single-channel optimization, shown in Figure 9(a), had an enhancement of $\eta = 348$ over background speckle. Multiple foci were also generated using Equation (50) and can be seen in Figures 9(b) and 9(c). As the energy is split between multiple foci the enhancement of each spot is reduced. For the two foci in Figure 9(b), the enhancement for the spots at $(72, 72)$ and $(96, 96)$ are $\eta = 47$ and 56, respectively. The enhancement for the three foci at $(72, 72)$, $(96, 96)$, and $(120, 120)$, shown in Figure 9(c), are $\eta = 26$, 32, and 29, respectively. As the enhancement decreases, the background speckle became more visible.

Simulations of scattering samples with larger correlations lengths were examined. By applying the same random phase value to groups of pixels in the simulated sample, lateral correlation lengths that are multiples of the minimum 20.6 μm can be simulated. In general, the larger correlation lengths did improve enhancement for some of the observation plane channels, but as the correlation length increased, the sample became more specular and the observation plane area where enhancement could be achieved became smaller. Doubling the lateral correlation length to 41.2 μm produced the best results with $N = 1,024$ SLM segments, and an observation plane of 768 by 768 pixels divided into $M = 16,384$ channels. The channels near the center of the observation plane achieved enhancement of $\eta \approx 1,000$, which is very near the predicted ideal maximum of Equation (10). The enhancement drops quickly as the channels move away from the center producing an average enhancement of $\eta_{avg} = 145$ for the 1,024 channels that were measured. Increasing the lateral correlation length beyond 41.2 μm did not significantly improve simulation results. In some cases the speckle patterns became less developed and unintended multiple foci were produced

that reduced overall enhancement as the simulated scattering sample became more specular.

4.3.2 Experimental Results.

Intensity measurements from the CCD are used to determine the RM. These measurements are sensitive to vibrations and changing environmental conditions in the laboratory. Thus, the faster the acquisition of the intensity measurements, the better the RM performs. The feedback from the CCD was limited to the center 512 by 512 pixels, which limits the observation area to 3.84 mm by 3.84 mm. Limiting the feedback area of the CCD both increased the frame rate and decreased the memory and computation time requirements to calculate the RM. The SLM was divided into $N = 1024$ segments. The feedback area from the CCD was segmented in $M = 4096$ channels, each channel was 8-by-8 pixels with a super-pixel area of 60 μm by 60 μm. The resulting RM was a matrix of 4096 by 1024 elements, which required a total of 4,104 intensity measurements, with an average run time under 300 seconds.

Single-channel optimization performance was measured by using the RM to sequentially refocus the beam to 1,024 of the available 4,096 CCD channels. The average single-channel enhancement was $\eta_{avg} = 9$ with a maximum enhancement of $\eta_{max} = 19$ over background speckle. Both single-channel and simultaneous multiple channel enhancement are shown in Figure 9(d), 9(e), and 9(f). Each spot location is labeled with its corresponding (row, column) coordinates. Single-channel enhancement at $(32, 32)$ is shown in Figure 9(d) with an enhancement of $\eta = 18$. Single-channel enhancement performance is less than 2% of the maximum ideal enhancement predicted by Equation (10) and less than 5% of the performance in the simulations. Multiple foci were generated along the diagonal using Equation (50) and are shown in Figures 9(e) and 9(f). Both foci in Figure 9(e) each have an enhancement of $\eta = 10$, while in Figure

9(f) the center spot enhancement is 6 and the two outer foci have an enhancement of 7 over background speckle.

The lower-than-anticipated enhancement can be partially attributed to non-ideal attributes of the laboratory equipment and environment such as SLM and CCD fill factors, vibrations, and temperature changes. The primary cause for the degraded enhancement performance is attributed to the lateral correlation length of the aluminum plate, which is assumed to be much less than the minimum simulated correlation length of 20.6 μm. A sample with a smaller lateral correlation length produces a higher degree of scattering that the SLM segments are not able to precisely match to produce the expected enhancement. Simply increasing the number of SLM segments is not likely to increase performance. The current experimental setup shown in Figure 2. It is the 2-dimensional spatial Fourier transform of the field at lens L_1 that is being scattered by the sample. The field at the lens is determined by propagating the field from the SLM to the lens. By increasing the number of SLM segments and decreasing their size, the spatial frequencies of the field at the lens are increased. Thus, the 2-dimensional spatial Fourier transform at the sample covers a larger area, further increasing the scatter and potentially decreasing overall enhancement.

The spatial Fourier transform of the field at the lens provided a linear, predictable, and convenient relationship for simulation purposes, but it does not minimize the interaction with the scattering sample. To improve enhancement using this relationship would require a large number of SLM segments (N), but the physical size of the segments would have to increase in order to minimize the size of the spatial Fourier transform at the sample. In Chapter V, reflective inverse diffusion experiments will attempt to increase enhancement by minimizing the interaction area of the light with the scattering sample.

4.4 Conclusion

Yoon's method for measuring transmission matrices has been demonstrated to work in reflection. The RM maintained the ability to refocus light to any of the individual channels of the CCD or multiple channels simultaneously. This method for measuring the RM required less than 20% of the intensity measurements of the previous iterative method of Section 2.3.2 that was only capable of optimizing to a single channel. The enhancement capabilities of the RM showed a dependence on the physical dimensions and total number of observation-plane channels (M) that was not mentioned in the case of transmission. The overall enhancement from the RM in the laboratory experiments was significantly less than anticipated and is attributed to a lateral correlation length of the scattering sample that is smaller than that which is able to be phase matched by the SLM. Spot enhancements of up to 20 times background speckle were achieved. Transmissive inverse diffusion experiments typically use optics to produce a de-magnified image of the SLM field at the transmissive sample and then re-magnify the scattered beam for imaging onto a CCD [5–7,14,15,17,19,21,33]. Chapter V will examine adapting this approach for use in reflection. Applying a de-magnified image of the SLM onto the scattering reflector could minimize the interaction area and improve the enhancement performance of the RM. However, implementing this approach in the application of imaging-around-corners could prove to be less practical than the focal-plane approach. None the less, improvement of the enhancement capabilities of the RM would provide a valuable tool for imaging using reflected light and effectively seeing around corners.

V. Reflection Matrix Measurement

5.1 Introduction

The majority of surfaces can be considered rough when compared to the wavelength of visible light. The microscopic surface height variations of the rough surface cause incident light to diffusely scatter. The scattering surface can be treated as a complex field that interferes with incident light to produce reflected speckle patterns. If the complex field of the rough surface was known, a properly modified incident beam could be used to eliminate the scattering effects of the rough surface and even cause the light to refocus after reflection [37].

Transmissive inverse diffusion used phase modulation to shape the wavefront of incident light causing it to refocus after transmission through a turbid media [5–7, 19, 30]. These methods were also demonstrated to work in controlling reflective scatter [9]. Reflective inverse diffusion is an iterative process with intensity feedback from a CCD to search for the SLM phase map that produced the brightest target spot in the observation plane. This required tens of thousands of intensity measurements and limited the phase map to a small subset of available values.

Transmission matrices have been developed to map the effect of the complex field of the scatterer on the incident light. These matrices provide the phase information required to control the resultant light scatter [14, 15, 21, 23]. Transmission matrices were measured with microscopic objectives and thin films of turbid media, resulting in propagation distance of less than 1 mm and a observation plane field of view of a few hundred microns. The complex field representation is not limited to transmissive scattering, but the reflective case represents a 10^3 increase in propagation distance and observation plane size. Initial work in reflective inverse diffusion always placed the rough surface reflector at the focus of a positive lens [9]. This paper will continue

to examine the enhancement capabilities of the RM with the rough surface reflector at lens focus. Additionally, the RM will be measured with the lens producing a demagnified image of the the SLM at the rough surface reflector, similar to the transmissive case.

Previous work in the transmissive scattering case showed enhancements (η) ranging from 50 to 1,000 using both iterative and tranmission matrix methods [6, 14, 19, 21, 34]. The cause of this wide range of enhancement values is still currently being investigated, with some of the disparity likely attributed to noise [34]. Enhancement capabilities of the RM in laboratory experiments and diffraction-based simulations are compared with surface roughness, correlation length, and slope to provide initial insight into surface characteristics that affect enhancement. The simulations will also examine the effect on enhancement of simplified device measurement error for the SLM and CCD along minute mechanical vibrations that cause microscopic shifts in the optical setup.

Imaging around corners using reflectively scattered light has tremendous application in remote sensing. Previous work in this area has always required the occluded scene to be illuminated by a light source either in the scene or with direct line of sight of the scene [2, 39]. This presents an application problem since access to the occluded scene may not be possible. The goal this RM research is to provide a method of illuminating the occluded target scene without access or direct line of sight.

5.2 Background

Transmissive and reflective scattering are both linear, deterministic processes as long as the scattering medium is static. In both cases, the resultant scattered field can be considered a linear combination of the inputs. Phase modulation using an SLM divides up the incident light into several several individual segments each with

a unique phase. Every sampled location in the observed speckle field is a linear combination of the field from the individual SLM segments. The field at the m^{th} segment of the observered field is given by Equation (1) and reprinted here [5],

$$E_m = \sum_{n=1}^{N} t_{mn} A_n e^{i\phi_n}, \tag{1}$$

where t_{mn} is the mn^{th} complex-valued element of the transmission/reflection matrix relating the light from the n^{th} SLM segment to the m^{th} segment in the observation plane, and $A_n e^{i\phi_n}$ represents the amplitude and phase of the light from the n^{th} SLM segment. Normalizing Equation (1) to intensity by setting $A_n = 1/\sqrt{N}$, the observed intensity was then given by Equation (2), also reprinted here,

$$I_m = |E_m|^2 = \frac{1}{N} \left| \sum_{n=1}^{N} t_{mn} e^{i\phi_n} \right|^2 . \tag{2}$$

Intensity enhancement (η) is a measure of performance for controlling scattered light. Defined in transmissive experiments as the ratio of the average intensity of the optimized segment, $\langle I_{opt} \rangle$, to the average intensity of the unoptimized random segments, $\langle I_{rnd} \rangle$ [7]. Assuming the surface height imperfections of the reflector are on the order of a wavelength and follow a Gaussian distribution, the reflector can be modeled as an average reflectivity with a uniform phase [10]. The reflector statistics can be used to show the expected maximum ideal enhancement, given in Equation (10) and reprinted here, is equal to N, the total number of SLM segments [9].

$$\eta = \frac{\langle I_{opt} \rangle}{\langle I_{rnd} \rangle} = N. \tag{10}$$

The method used to measure the RM was based on work by Yoon *et al.* for measuring transmission matrices of turbid media [17]. Yoon's method was based on parallel wavefront optimization method by Cui and expanded to measure the entire

transmission matrix, rather than optimize to a single point [17,19]. Parallel wavefront optimization uses interference between reference and signal fields produced by the SLM to extract the phase information of the RM [17, 19]. The SLM segments are divided into two groups, the Group 1 segments are modulated at a separate frequency to produce the signal field, and the Group 2 segments are static, producing the reference field. The intensity of a segment in the observation plane is a combination of the reference and signal fields and was given by Equation (42), also reprinted here [17],

$$\begin{aligned} I_m = |E_m|^2 &= \left| \sum_{n=G+1}^{N} t_{mn} + \sum_{p=1}^{G} t_{mp} e^{j\omega_p t} \right|^2 = \left| R_{m2} + \sum_{p=1}^{G} t_{mp} e^{j\omega_p t} \right|^2 \\ &= |R_{m2}|^2 + R_{m2}^* \sum_{p=1}^{G} t_{mp} e^{j\omega_p t} + R_{m2} \sum_{p=1}^{G} t_{mp}^* e^{-j\omega_p t} + \sum_{p=1}^{G} \sum_{q=1}^{G} t_{mp}^* t_{mq} e^{j(\omega_q - \omega_p)t}, \end{aligned} \tag{42}$$

where R_{m2} is the sum of the static Group 2 segments that produce the reference field. The second term of Equation (42) shows the matrix coefficients, t_{mp}, occur at discrete frequencies. The $(R_{m2}^* t_{mp})$ coefficients can be extracted using the temporal Fourier transform of the segment intensity. This process produces half of the matrix coefficients, the roles of the SLM segments are then switched to capture the other half of the RM coefficients. A third optimization is performed to bring both halves of the RM into phase [17].

5.3 Methodology

5.3.1 Laboratory Experiments.

The primary equipment for the laboratory experiment is a laser source, an SLM, and a CCD for feedback. The laser source is a Thorlabs 5-mW HeNe laser ($\lambda = 632.8$

nm) with a linearly polarized output. The laser is beam expanded to fully illuminate the SLM. The Meadowlark P512 is a LCoS SLM consisting of 512×512 pixels, each capable of over 16,000 discrete phase levels over a total 2π phase stroke. The SLM has an effective area of 7.68 mm $\times$ 7.68 mm with pixel pitch of 15 μm. Intensity feedback is recorded using a Thorlabs 4070-GE monochrome CCD detector array with a resolution of 2048×2048 pixels and a pixel pitch of 7.5μm.

A total of five rough-surface samples were made from 1-inch aluminum squares. Each sample received a different surface preparation, the first was bead blasted, while the remaining four were polished with 100 grit, 220 grit, 320 grit, and 600 grit sand paper. Surface profiles of each sample was measured using a Tencor stylus profiler in both the x and y directions. The surface roughness, σ, was calculated as the standard deviation in surface height in each direction and then averaged together to produce a single roughness value per sample. The sample roughness and autocorrelation length is in Table 2.

The RM of each sample was measured in three separate locations using the optical setup shown in Figure 2. This is the same optical setup used in the original reflective inverse diffusion experiments with the rough surface reflector was placed at the focus of lens L_1 [9]. The reflection matrix measurements were repeated using the optical setup shown in Figure 10. The single lens system produced a $\frac{1}{8}$-scale image of the SLM on the rough-surface reflector. The reflection matrix was then used to refocus light individually to each of the M segments of the observation plane. The average and maximum intensity enhancements for each sample are also shown in Table 2.

5.3.2 Simulations.

The propagation model assumes the SLM is illuminated by a unit amplitude ideal plane wave. The individual SLM segments are represented by unimodular complex

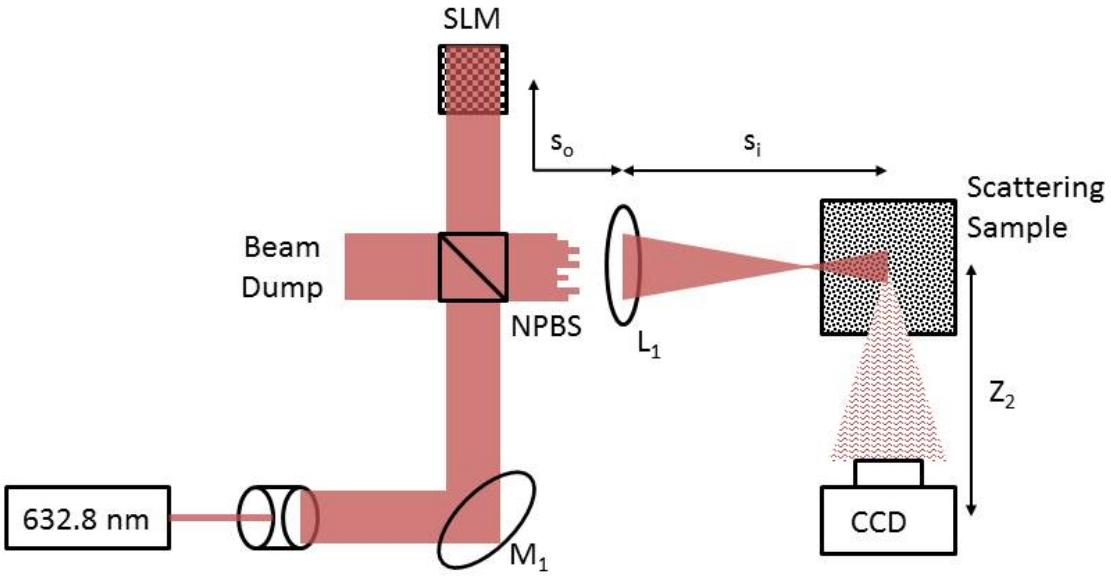

Figure 10. Image plane optical setup for reflective inverse diffusion. A vertically polarized HeNe laser is expanded, collimated, and normally incident on the SLM. The lens (L_1) produces a demagnified image of the phase modulated beam onto the rough surface reflector and the reflected speckle pattern is recorded by the CCD. The mirror (M_1) and the NPBS are used to allow normal incidence with the SLM. The demagnification of the system is $\frac{s_i}{s_o} \approx \frac{1}{8}$.

coefficients. The phase of these coefficients represents the phase delay imparted by the SLM segments onto the incident plane wave. Absorption and transmission are neglected when modeling the aluminum rough-surface reflectors; thus, the samples are also modeled as unimodular complex numbers. The random phase imparted by the rough surface is related to the surface height fluctuations or surface roughness. Assuming a Gaussian surface height distribution with a standard deviation equal or greater than $\lambda/2$, the phase distribution becomes uniform when wrapped to the interval $[-\pi, \pi]$ [10].

Diffraction-based models were simulated using the MATLAB® 2-dimensional fast Fourier transform (FFT) and the Rayleigh-Sommerfeld transfer function [36]. For the focal-plane optical setup in Figure 2, the complex field at the observation plane is calculated using the Rayleigh-Sommerfeld transfer function and spatial Fourier transform property of the lens. The field in the observation plane was given by Equation 38 and reprinted here [9],

$$U_{CCD}(u,v) = \mathcal{F}^{-1}\{\mathcal{F}\{e^{j\frac{k}{2f}(u^2+v^2)}e^{j\theta(u,v)}\mathcal{F}\{U_{SLM}(x,y)\}H(f_x,f_y)|_{z=Z_1}\}\, H(f_u,f_v)|_{z=Z_2}\}, \tag{38}$$

where (x, y) are the coordinates of the source plane at the SLM and (u, v) are the coordinates of the sample plane at the lens focus. The horizontal and vertical spatial frequencies of the source and sample planes are (f_x, f_y) and (f_u, f_v), respectively. The focal length of lens L_1 is f, and z_1 and z_2 are the distances from the SLM to the lens and from the reflective sample to the CCD, respectively. The rough surface is represented by $e^{j\theta(u,v)}$, where the phase function $\theta(u, v)$ is a random uniform distribution from $[-\pi, \pi]$.

Ideal imaging is assumed for the configuration in Figure 10. Propagation from the

SLM to the rough sample is reduced to a global phase shift and can be ignored. The rough surface then randomizes the phase of the ideal image, which is then propagated to the CCD in the observation plane using the Rayleigh-Sommerfeld transfer function. Thus the field in the observation plane is given by,

$$U_{CCD}(u,v) = \mathcal{F}^{-1}\{\mathcal{F}\{e^{j\theta(u,v)}U_{SLM}(\frac{s_o}{s_i}u, \frac{s_o}{s_i}v)\}H(f_u, f_v)|_{z=z_2}\} \tag{52}$$

where s_o is the object distance from the SLM to the lens L_1, and s_i is the image distance from the lens L_1 to the rough surface sample. The MATLAB® source code for the simulations is available in Appendix A.

5.3.3 Segment Size.

The number of SLM segments, N, is directly proportional to the maximum ideal enhancement of the refocused spot on the CCD. The parallel wavefront modulation method used to measure the RM requires $4N + 8$ intensity measurements [17]. For all the experimental RM measurements, the SLM was divided into 1,024 equal-sized segments, arranged 32×32, which required 4,104 intensity measurements to measure the RM. This was the largest number of segments that could be equally sized and utilized the entire SLM area.

The segment size of the CCD also affects enhancement. Parallel wavefront modulation measures the RM in two separate halves. If the CCD segment size is too large, the two halves of the RM may focus to separate locations within the same CCD segment resulting in a larger blurred spot with lower overall enhancement. The only indication of a CCD segment that is too large is the lack of enhancement increase during the third step of parallel wavefront optimization, phase matching the two halves of the RM. Selecting a CCD segment size that is smaller than necessary increases the total number to segments and increases the memory and processing time of the

RM measurement. The best CCD segment size was found to be approximately 1/2 the size of the predicted diffraction-limited spot of the optical system.

The predicted spot size for the optical system shown in Figure 2 was calculated in the original reflective inverse diffusion proof-of-concept experiments [9]. The radius of the final spot was given by,

$$q_2 \approx \frac{z_2}{f}\frac{D_{SLM}}{2\sqrt{N}}, \tag{53}$$

where z_2 is the distance from the sample to the CCD, f is the focal length of lens L_1, D_{SLM} is the width of the SLM, and N is the total number of SLM segments. Using Equation (53), the CCD segment size for the focal-plane optical setup is 120 μm, which is 16×16 pixels on the Thorlabs 40740M CCD.

The predicted spot size for the imaging system in Figure 10 is calculated as the diffraction-limited spot produced by an aperture the size of the demagnified SLM image that is applied to the rough-surface reflector. The radius of the final spot is then given by,

$$q_2 \approx \frac{\lambda z_2}{\frac{s_i}{s_o}D_{SLM}} = \frac{s_o}{s_i}\frac{\lambda z_2}{D_{SLM}} \tag{54}$$

where s_o is the object distance from the SLM to lens L_1, and s_i is the image distance from lens L_1 to the rough surface sample. Thus the segment size for the imaging system is 317 μm, which is 42×42 pixels on the Thorlabs 4070M CCD.

5.4 Results and Analysis

5.4.1 Experiments.

The RM was measured three times along the diagonal of each sample, top left corner, center, and bottom right corner, for both the focal-plane and imaging optical

systems. The RM was then used to focus the incident beam to 1,024 different segments of the CCD and record the enhancement of each target segment over the background segments. The maximum enhancement for each sample, η_{max}, is the average peak enhancement from each of the three measured RMs. The average enhancement for each sample, η_{avg}, is the mean enhancement value over all the segments from all three RMs. The η_{max} and η_{avg} for each of the five samples are recorded in Table 2.

Table 2. Summary table for the five aluminum samples. Roughness (σ) is the standard deviation of the sample surface height. Correlation (ℓ_c) is the autocorrelation shift to reduce the maximum value by e^{-1}. Slope (s) is the RMS surface slope. Correlation ($\ell_{\lambda/2}$) is the lateral distance required to change the surface height by $\lambda/2$ at the RMS slope (s). The samples average enhancement (η_{avg}) and maximum enhancement (η_{max}) achieved with each optical setup are included.

Aluminum	Roughness	Correlation	Slope	Correlation	Focal Plane		Image Plane	
Samples	σ	ℓ_c	s	$\ell_{\lambda/2}$	η_{avg}	η_{max}	η_{avg}	η_{max}
100 Grit	2.13 μm	54.25 μm	0.143	2.21 μm	1.6	7.2	2.2	10.1
220 Grit	1.67 μm	35.25 μm	0.141	2.24 μm	1.5	5.8	3.1	13.3
Bead Blasted	1.04 μm	30.25 μm	0.105	3.00 μm	2.2	8.5	6.1	22.5
320 Grit	0.63 μm	13.75 μm	0.107	2.97 μm	1.3	4.5	4.3	16.7
600 Grit	0.45 μm	16.00 μm	0.066	4.79 μm	1.3	6.0	5.4	24.2

Data trends in Figure 11 show enhancement decreases as surface roughness increases for the imaging system. The enhancement for the focal-plane system is almost flat with the average enhancement just slight larger than 1; i.e. the target segment intensity is not significantly higher than the background. The difference between constructive and destructive interference is a surface height change of $\lambda/2$; thus, the rate at which the surface height changes is a better predictor for enhancement. The root mean square (RMS) surface slope indicates the rate of the surface height fluctuations and was determined from the profile data from each sample. For discrete profile data, the surface slope is given by [11],

$$s = \left[\frac{1}{K-1} \sum_{k=1}^{K-1} \left(\frac{z_k - z_{k-1}}{x_k - x_{k-1}} - \hat{z'} \right)^2 \right]^{\frac{1}{2}} \tag{55}$$

where K is the total number of measurements, z_k is the surface height from the

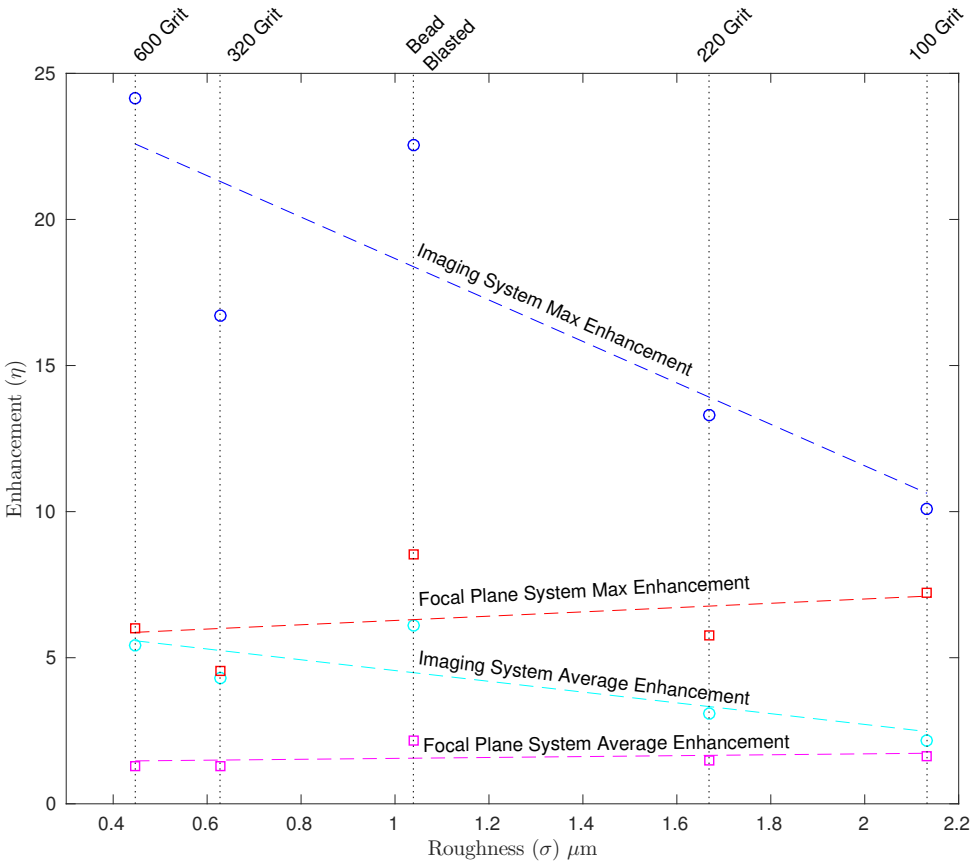

Figure 11. The surface roughness measured by the Tencor profilometer is plotted with enhancement. Linear trend lines were added. For the focal plane system, maximum enhancement is shown in red, while average enhancement is shown in magenta. For the imaging system, maximum enhancement is shown in blue, while average enhancement is shown in cyan.

profilometer, x_k is the lateral sample distance, and $\hat{z}' = \frac{z_K - z_1}{K\Delta x}$ is the average slope. The RMS slopes of the samples are included in Table 2. In general, the samples with larger RMS slope showed lower enhancement.

The correlation length, ℓ_c in Table 2, is defined as the shift required to lower the autocorrelation of the surface height profile by a factor of e^{-1} of the maximum value [11]. The apparent inverse relationship between correlation length and enhancement is counter-intuitive, but is not conclusive since the samples with the longest correlation length also have the highest roughness. None of the samples showed Gaussian surface-height distributions, and with regards to reflective inverse diffusion, the standard e^{-1} definition used for correlation length is overly optimistic due to the small surface-height difference between constructive and destructive interference.

For reflective inverse diffusion the proposed lateral dimension, $\ell_{\lambda/2}$ in Table 2, is defined as the distance required to achieve a $\lambda/2$ change in surface height given the RMS slope. Enhancement is plotted with $\ell_{\lambda/2}$ in Figure 12. The imaging system showed enhancement increases with $\ell_{\lambda/2}$. The data is inconclusive in the focal-plane system due to low enhancement values and virtually flat trends.

5.4.2 Simulations.

The RM produced by the simulation of the focal-plane system in Figure 2 was used to refocus the incident beam to 1,024 of the 16,384 observation plane segments. The rough surface reflector was made up of individual segments with a uniform phase distribution. The phase of each segment was independent which leads to a delta correlated sample. The segment size is a measure of lateral correlation, but due to the phase independence between each segment, it was not directly comparable to ℓ_c of the tested aluminum samples.

The phase of the simulated rough surface segments is a uniform distribution over

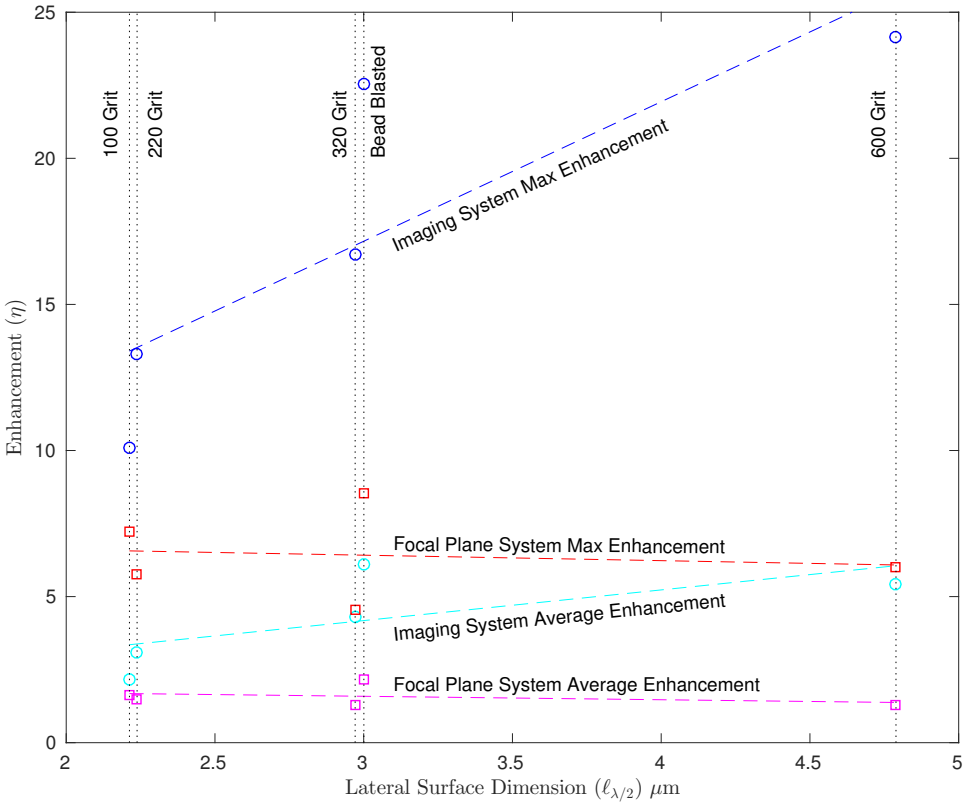

Figure 12. The lateral surface dimension $\ell_{\lambda/2}$ is plotted with enhancement. The focal-plane system shows no change in enhancement with $\ell_{\lambda/2}$. However, the average enhancement of 1 indicates the target segment has the same intensity as the background.

$[-\pi, \pi]$. If bounded over a single wavelength, the phase distribution gives a surface height range from $[-\frac{\lambda}{2}, \frac{\lambda}{2}]$. Since the simulated rough surface segments are independent, the surface height difference $(z_k - z_{k-1})$ in Equation (55) for surface slope, is a random variable with the same uniform distribution and an expected value of $\lambda/2$. Assuming a mean slope of $\hat{z}' = 0$, the RMS surface slope for the simulated rough surface is given by,

$$s_{sim} = \left[\frac{1}{K-1} \sum_{k=1}^{K-1} \left(\frac{E[z_k - z_{k-1}]}{\Delta x} \right)^2 \right]^{\frac{1}{2}} = \left[\frac{1}{K-1} \sum_{k=1}^{K-1} \left(\frac{\lambda/2}{\Delta x} \right)^2 \right]^{\frac{1}{2}} = \frac{\lambda}{2\Delta x} \qquad (56)$$

where Δx is the dimension of the simulated rough surface sample segment. Given the of the surface slope in Equation (56), for the simulations $\ell_{\lambda/2} = \Delta x$, the simulated rough surface segment size.

The simulated SLM was zero-padded as described in section 3.4 to produce a lateral surface dimension ($\ell_{\lambda/2}$) of 10.3 μm. Decreasing the lateral surface dimension below 10.3 μm caused unacceptable increases to processing time. Larger lateral surface dimensions were simulated by setting groups of pixels to the same value. Ultimately lateral surface dimensions from 10.3 μm to 660 μm were simulated. Maximum enhancement was achieved with $\ell_{\lambda/2} = 41$ μm, which produced an enhancement of $\eta_{max} = 907$ or 88% of the predicted ideal maximum from Equation (3). The best average enhancement of the 1,024 simulated measurements was achieved with $\ell_{\lambda/2} = 82$ μm, which produced an enhancement of $\eta_{avg} = 708$. Increasing $\ell_{\lambda/2}$ beyond 82 μm caused both the maximum and average enhancements to decrease.

In the focal-plane system, the individual SLM segments act as individual apertures. The spacing and phase of the SLM segments create fringe patterns in the diffraction limited spot incident on the rough surface reflector. The sum of all interferences from the SLM segment pairs produces a wavefront that conjugates the phase

imparted by the rough surface reflector to produce a wave that converges in the observation plane. Segment pairs that are furthest apart produce the narrowest fringe spacing of 41 μm. This represents the smallest lateral surface dimension ($\ell_{\lambda/2}$) that the focal-plane system can conjugate and explains the peak maximum enhancement at 41 μm for the focal-plane system, see Figure 13. Using the RM to refocus light ensures that the light at the target segment is all in-phase, but it does not guarantee it is the only segment where the light is in-phase. In the focal-plane system, as the correlation length of the simulated sample increased, higher-order fringes would be incident on the same simulated sample segment and remain in-phase. This produced additional foci in the observation plane that would increase background intensity and decrease enhancement as the correlation length was increased, see Figure 13.

Simulations of the imaging system shown in Figure 10 assumed a 1-mm^2 ideal image of the SLM projected onto the rough-surface reflector. The SLM was modeled with N=1,024 equal-sized segments, arranged 32 $\times$ 32 across the SLM, each with an area of 31.25 μm $\times$ 31.25 μm. The lateral surface dimension of the simulated SLM image is the dimension of a single SLM segment, $\ell_{\lambda/2,SLM} = 31.25$ μm. The rough-surface reflector was modeled with discrete segments, all with unit magnitude and a uniform phase distribution. The $\ell_{\lambda/2}$ of the simulated rough surface was adjusted by varying the number of segments used in the model. Simulations were performed with rough-surface lateral dimensions ($\ell_{\lambda/2}$) as high as 500 μm, and as low as 7.8 μm.

When the lateral surface dimension of the simulated rough surface was identical to the lateral surface dimension of SLM image, $\ell_{\lambda/2} = \ell_{\lambda/2,SLM}$, the simulated RM achieved a maximum enhancement of $\eta_{max} = 673$ with an average enhancement of $\eta_{avg} = 310$. This represents 30%-65% of the performance predicted by Equation (3). This performance drops to 28%-39% as the correlation length of the rough surface decreases to $^1/_4$ of the correlation length of SLM image. The best performance of

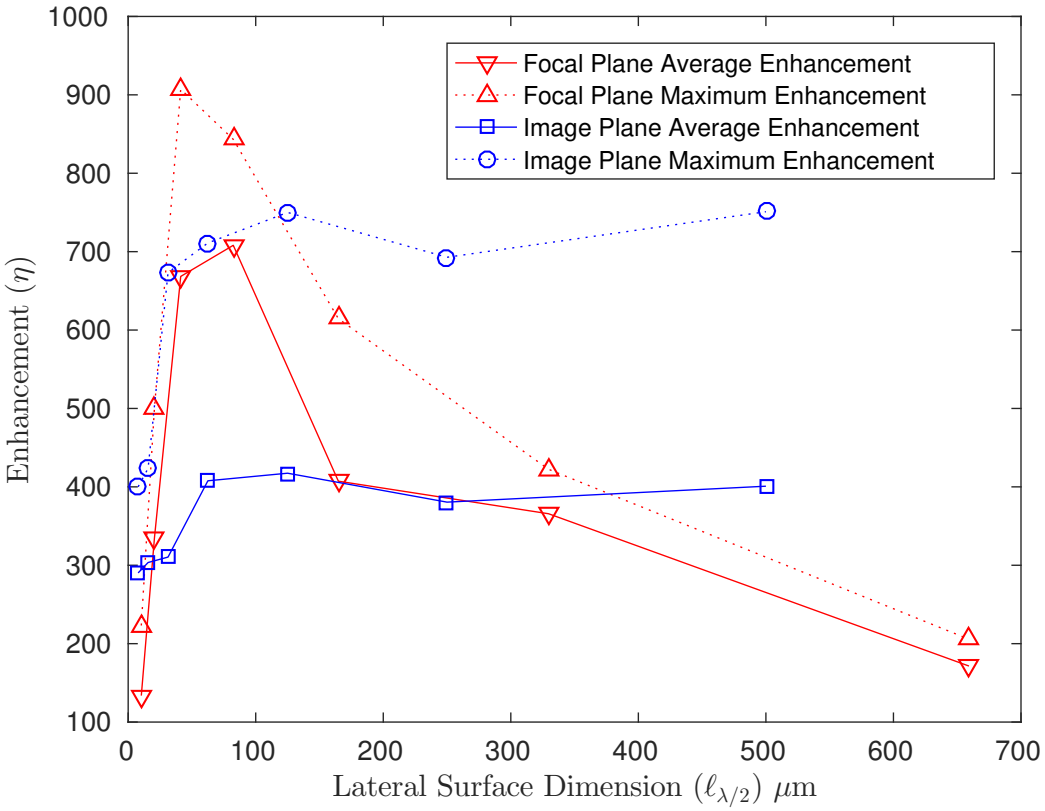

Figure 13. Simulated correlation length $\ell_{\lambda/2}$ vs enhancement. The red solid line shows average enhancement of the focal-plane system, where the red dotted line shows maximum enhancement. The solid blue line shows average enhancement of the imaging system, with the blue dotted line representing maximum enhancement.

40%-73% was achieved when $\ell_{\lambda/2} = 4\ell_{\lambda/2,SLM}$.

The simulations with the longer lateral surface dimension ($\ell_{\lambda/2}$) produced greater enhancement, both the maximum achieved by a single observation plane segment, and the average enhancement of the simulated 1,024 observation-plane segments. The enhancement is plotted with lateral surface dimension ($\ell_{\lambda/2}$) for both the focal-plane and imaging systems in Figure 13. The focal-plane system achieves much higher peak enhancement, but only at very specific correlation lengths before it rapidly decreases. The imaging system out performs the focal-plane system at shorter values of $\ell_{\lambda/2}$ in both maximum and average enhancement. For longer values of $\ell_{\lambda/2}$ the enhancement of the imaging system remains stable and does not decrease.

In the imaging case, the SLM is imaged and directly applied to the rough surface reflector. The SLM segments conjugate the phase changes imparted by the reflector and produce a converging wavefront. As the lateral surface dimension ($\ell_{\lambda/2}$) of the sample increases, fewer adjustments to the phase map are required. Extended to the perfect mirror case, the SLM phase map becomes the discretized phase function for a positive lens with the focal length in the observation plane. The background intensity does not increase with correlation length as in the focal-plane system. As correlation length increases, diffraction from the SLM segments and phase quantization error of the SLM becoming the limiting factors for enhancement.

5.4.3 RM properties.

The RM measured with the focal-plane and imaging systems both maintained the ability to refocus light to a single CCD segment or multiple segments simultaneously similar to their transmission matrix counterparts. Multiple segments are enhanced simultaneously using the same process as the transmission case, by using a linear combination of the rows of the RM [17]. Simulations of the focal-plane system show

single-segment enhancement in Figure 9(a), and multi-segment enhancements shown in Figures 9(b) and 9(c). The imaging system with the 600-grit aluminum sample demonstrates single-segment and simultaneous multi-segment enhancements and are shown in Figures 14(d), 14(e), and 14(f). Each spot location is labeled with its corresponding (row, column) coordinates. As the enhancement was split over multiple segments, the background intensity becomes more visible.

5.4.4 Predicted vs Measured Enhancement.

The best enhancement values from the aluminum samples were 10 to 24 times the RMS background intensity, which is less than 10% of the average enhancement of 300 to 400 achieved in simulation. Device error does not account for this discrepancy. For both the imaging and focal-plane simulations, including a random device error up to 5% for both the SLM and the CCD only decreased the average enhancement by approximately 10%. The RM is measured using the temporal FFT of intensity measurements from the CCD. This makes the measurement process inherently noise resistant since random device noise does not occur at a specific frequency.

The aluminum samples are assumed to be stable for much longer than the 5 minutes it takes to measure the RM. However micro-vibrations in the optical setup cause the incident light to shift on the rough surface reflector. The oscillation of the RM measurement area produces intensity measurements that belong to several different RMs. For the imaging system with a simulated rough surface lateral dimension of $\ell_{\lambda/2} = 7.8$ μm, incorporating a random vertical and horizontal shift of the sample of 23.4 μm reduces average enhancement to $\eta_{avg} = 6$ and maximum enhancement to $\eta_{max} = 43$. For the focal-plane system with a simulated rough surface lateral dimension of $\ell_{\lambda/2} = 10.3$ μm, a simulated vibration magnitude of 20.6 μm produces maximum enhancement of $\eta_{max} = 12$ and an average enhancement $\eta_{avg} = 2.3$.

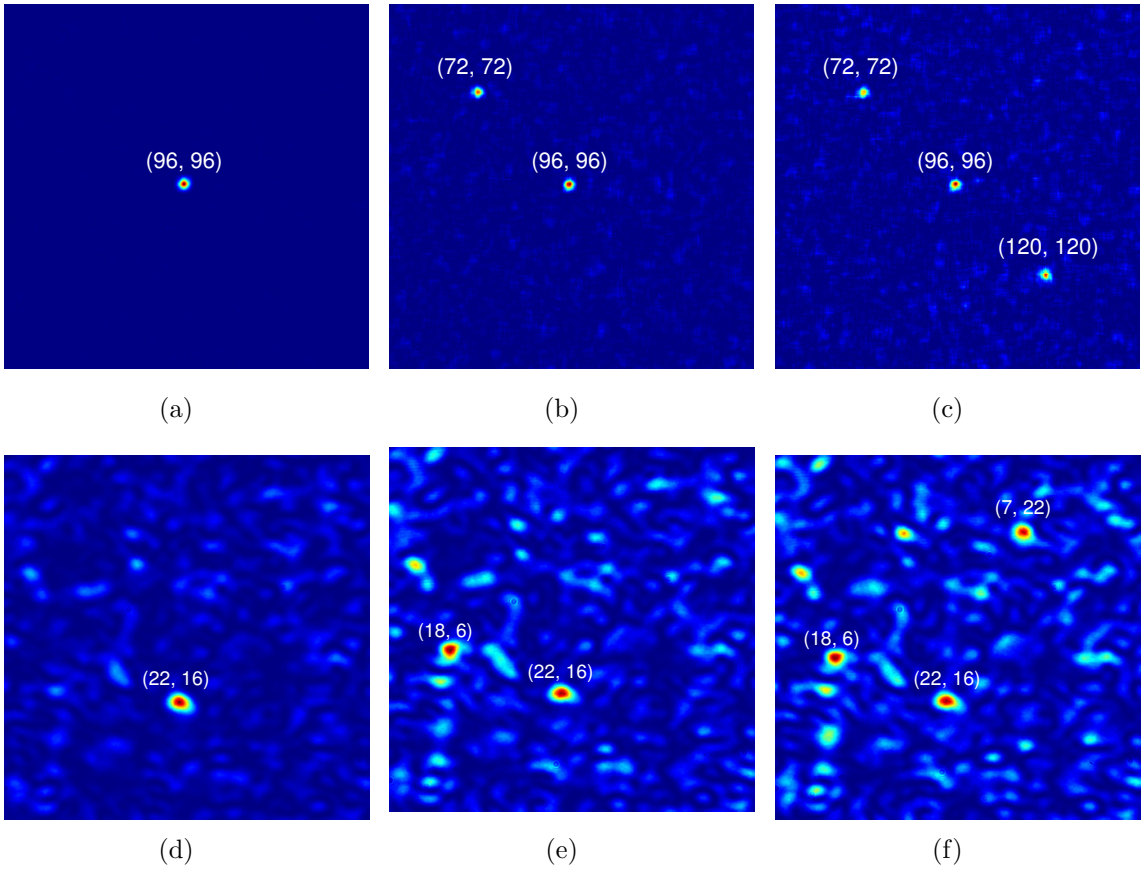

Figure 14. Observation plane intensity patterns (a)-(c) are computer simulations of the focal-plane system and (d)-(e) are laboratory results of the imaging system in Figure 10 with the 600-grit aluminum sample. Above each spot are the (row, column) coordinates of the given observation plane segment. Phase maps generated by the RM are used to refocus light to single or multiple segments in the observation plane. (a) A simulated single-segment enhancement of $\eta = 348$ over background speckle. (b) Simulation of two foci optimized simultaneously at $(72, 72)$ and $(96, 96)$ with enhancements of $\eta = 47$ and 56, respectively. (c) Simulation of three foci generated with increased background speckle at $(72, 72)$, $(96, 96)$, and $(120, 120)$ with enhancement values of $\eta = 26$, 32, and 29, respectively. (d) Demonstrated single-segment enhancement of $\eta = 12$ over background speckle. (e) Two segments are optimized simultaneously, measured enhancement for both foci is $\eta = 6$. (f) Three foci are generated with increased background speckle at $(18, 6)$, $(22, 16)$, and $(7, 22)$, enhancement values are $\eta = 6$, 5, and 5, respectively.

The lateral surface dimension ($\ell_{\lambda/2}$) for the aluminum samples is much smaller than can be simulated without an exponential increase in processing time. However, trends between enhancement and $\ell_{\lambda/2}$ from the experiments and simulations were extended and plotted for comparison in Figure 15. The imaging system shows the best alignment between experimental and simulation trends for maximum enhancement. The imaging system average enhancement trend lines for experimental and simulation data have matching slope despite the increase in separation. The experimental data for the focal-plane system showed very low enhancement with predominately flat trends for both average and maximum measured enhancement. Similar enhancement levels are achieved in simulation for $\ell_{\lambda/2} = 10.3$ μm with the addition of the random vibration oscillation of 20.6 μm. Simulations show enhancement increases for $\ell_{\lambda/2} > 10.3$ μm. This could indicate the correlation length of the aluminum samples was too small for the focal-plane system to be effective in the given laboratory conditions.

5.5 Conclusion

Yoon's method for measuring transmission matrices was successfully implemented to measure a reflection matrix (RM). The method only requires the optical system to be linear. Both the focal-plane and the imaging systems produced RMs capable of refocusing light onto the CCD. The RM is capable of enhancing a single CCD segment, or multiple segments simultaneously.

Simulations show the focal-plane system achieving higher levels of enhancement for a very specific lateral surface dimension ($\ell_{\lambda/2}$). Outside of this optimum range, the imaging system produces better enhancement. Laboratory data shows the imaging system consistently produced higher levels of enhancement than the focal-plane system on all the samples tested. This was expected as simulations predicted the imaging system would achieve higher levels of enhancement at lower values of $\ell_{\lambda/2}$.

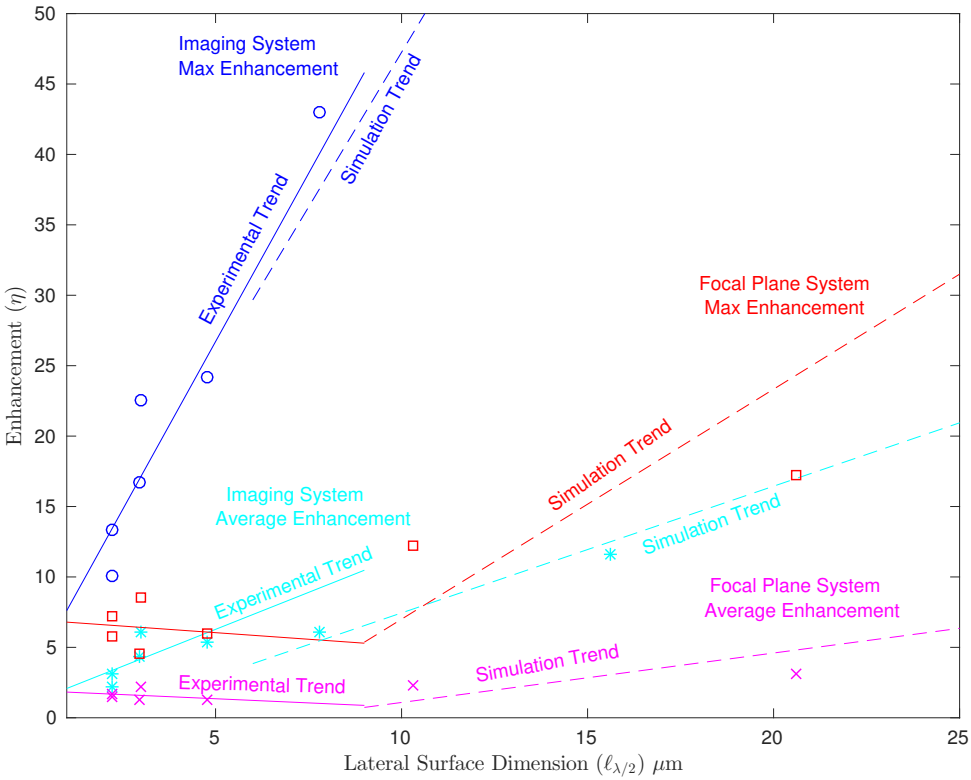

Figure 15. Simulations are conducted with a random shift in the sample prior to each intensity measurement. The solid lines are experimental data trends, dashed lines represent simulation data trends. The simulated focal-plane system is subject to a random 20.6 μm shift, maximum enhancement is shown in red, while average enhancement is shown in magenta. The simulated imaging system is subject to a random 23.4 μm shift, maximum enhancement is shown in blue, while average enhancement is shown in cyan.

The enhancement for both the focal-plane system and imaging system was significantly lower than predicted by Equation (10) for the ideal simulated results. The primary cause of this was minute mechanical vibrations in the optical setup. Although enhancement for both methods were affected, incorporating a simple random vibration in the simulation model showed that the imaging system was capable of greater enhancement values in this non-ideal case. This is corroborated by the higher enhancement values achieved by the imaging system in the laboratory.

Further research is required to solidify the RM measurement method. Improving the vibration isolation of the optical system will be key to improving the RM enhancement performance. Mathematical methods for combating the effects of vibration, such as dynamic data driven applications systems (DDDAS) [40], should also be explored as a more cost effective solution. Ideally, in the imaging case, the incident light is scattered by the same part of the rough surface regardless of the which CCD segment is enhanced. Since the rough surface is assumed to be static, the scattering is deterministic [5]. Chapter VI will investigate methods of exploiting the deterministic process to determine methods of reconstructing missing portions of the RM from partial data, or expanding an RM to include additional CCD segment locations without requiring the RM to be re-measured.

VI. Reflection Matrix Reconstruction

Every row of the reflection matrix (RM) contains the information necessary to produce a converging wave after reflection off the rough-surface reflector. Assuming the reflector properties are static and the incident light always interacts with the same portion of the reflector surface, the scattering process is deterministic, which means every row of the RM also contains surface height information about the rough-surface reflector. Since the light interacts with the same surface area for a given RM, the phase information that conjugates the phase changes imposed by the surface is the same for all the rows of the RM. Thus, a large amount of the information in the RM is redundant, which can be exploited.

The imaging system that was introduced in Chapter V produced greater levels of maximum and average enhancement at smaller lateral surface dimensions ($\ell_{\lambda/2}$) than the original focal plane system of Chapter II. The enhancement of the imaging system also remained stable as $\ell_{\lambda/2}$ was increased. The imaging system also provided a direct application of an SLM phase map to the rough-surface reflector, which simplified pattern analysis of the RM. Thus, the methods in this chapter have been developed for use with the imaging system. However, these methods should be adaptable to the focal plane system provided the method is modified to account for the spatial Fourier transform relationship between the SLM and the rough-surface reflector.

6.1 Geometric Analysis

Reflective inverse diffusion is based on the SLM ability to compensate for the surface height fluctuations of the rough-surface reflector and cause the light to refocus at a desired point in the observation plane. The phase maps produced by the RM can be considered in two parts that are added together and phase wrapped over $[-\pi, \pi]$.

The first part of the phase map produces the converging phase front matching a discretized phase function for a positive lens. The second part of the phase map conjugates the phase shifts caused by the surface height fluctuations of the rough-surface reflector. The rough surface behaves as a flat smooth specular surface that reflects the remaining converging phase front produced by the phase map like a mirror.

Steering the focused spot to an adjacent observation plane segment requires a 625-μrad change to the angle of reflection to shift the focused spot 312.5 μm in the observation plane located 0.5 m from the reflector. Physically changing the incident angle of the system is impractical because the incident beam would shift location on the reflector and invalidate the RM. The path length difference caused by the small change in incident and reflection angle can be expressed as a linear phase shift and added to the existing phase map of the RM. Using the small-angle approximation, the path length is linear from 0 to 625 nm across the 1-mm demagnified SLM image projected onto the rough-surface reflector. Thus, to shift the target segment to an adjacent segment in the observation plane requires a linear phase shift from 0 to almost 2π, or approximately one full wavelength.

6.2 Reflection Matrix Analysis

The RM generated from ideal simulations was found to contain linear phase shifts between the rows of the RM representing adjacent observation plane segments. The phase shift was comparable to the result from the geometric analysis: a linear, 0-to-2π phase shift, over the width of the simulated SLM. The difference between two phase maps from the RM that each refocuses the light to vertically adjacent observation plane segments is shown in Figure 16(a); for two horizontally adjacent observation plane segments, the phase map difference is in Figure 16(b). Phase maps for $x-$ and $y-$tilt calculated using the geometric approximation are shown in Figures 16(c) and

16(d). The phase maps are similar to the first-order Zernike polynomials for tilt [41]. However, since orthogonality is not a concern, a circular aperture is not required. This phase map can be applied to shift the focus spot to an adjacent target segment in the observation plane. The linear phase difference was consistent throughout the entire RM, so it is possible to reconstruct a new RM from a single row from an existing RM.

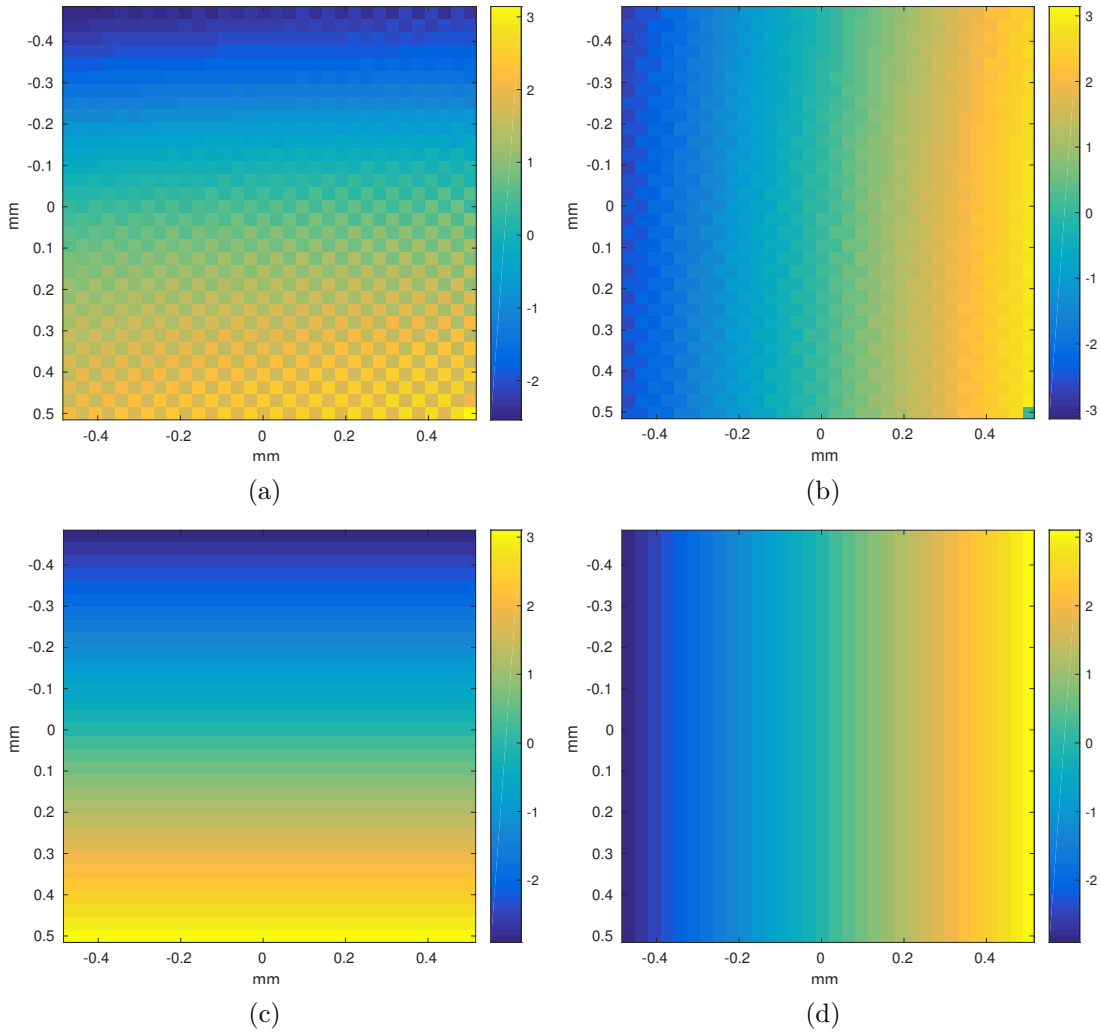

Figure 16. (a) Phase map difference from two rows of the RM corresponding to vertically adjacent observation plane segments. (b) Phase map difference from two rows of the RM corresponding to horizontally adjacent observation plane segments. (c) Phase map calculated from geometric analysis to shift target observation plane segment to the adjacent segment below. (d) Phase map calculated from geometric analysis to shift target observation plane segment to the adjacent segment to the right.

A single row from an existing RM is a phase map that refocuses light after reflec-

tion to a specific segment in the observation plane. A new RM can be constructed by using the tilt phase maps in Figure 16 to calculate phase maps for the adjacent observation-plane segments. This is repeated until the entire RM is reconstructed. In ideal simulations, the enhancement performance of the new RM is dependent on the enhancement achieved by the original reference phase map used in construction. The original RM from an ideal simulation produced an average enhancement (η_{avg}) of 310 and a maximum enhancement (η_{max}) of 677. A reference phase map was selected from this RM that produces an enhancement (η) of 304. From this phase map, a new RM was constructed that produced $\eta_{avg} = 306$ and $\eta_{max} = 546$, approximately a 20% decrease in maximum enhancement. Using a reference phase map that produced an enhancement of 658, the reconstructed RM performance was $\eta_{avg} = 503$ and $\eta_{max} = 776$, representing 62% and 15% increases, respectively. The RMS difference between the new RM and the reconstructed RM was greater than $\frac{\pi}{2}$ for all the conducted ideal simulations. This would indicate that there exist many RMs for a given random rough surface reflector and the parallel wavefront modulation method used for measuring the RM does not guarantee the best enhancement performance.

6.3 Vibrational Noise

Vibrations in the optical setup severely limited the enhancement performance of the RMs measured in the laboratory. These vibrations obscured linear phase tilt differences between phase maps for adjacent CCD segments. Adding a random vibrational shift of 30 μm to the simulations made the linear phase tilt difference that was present in the ideal simulations all but indistinguishable. However, even under these non-ideal circumstances, the method for reconstructing a new RM from a single phase map is still valid. The original RM with a 30-μm vibration produced $\eta_{avg} = 4$ and $\eta_{max} = 20$. Using a phase map that produced an enhancement of 20, the

new rescontructed RM performance was increased to $\eta_{avg} = 7$ and $\eta_{max} = 21$, which represents a 75% increase in average enhancement.

6.4 Conclusion

The imaging system developed for measuring a RM directly applied the phase of the SLM to the rough surface reflector which allowed new phase maps to be calculated by applying a linear phase tilt to shift the target segment in the observation plane. A similar process should be possible with the focal-plane system by applying the inverse spatial Fourier transform of the tilt phase maps in Figure 16. However, this was not explored due to the superior performance of the imaging system and time constraints. Still, it should be explored as future work.

Ideal simulations show that reconstructed RM enhancement performance is dependent on the enhancement of the reference phase map used in the construction. It was demonstrated that in some cases, the reconstructed RM can out-perform the original. The RMS phase difference between the original and reconstructed RM indicates that multiple RM may exist for a given surface. The increased performance of the reconstructed RM indicates that parallel wavefront modulation method does not guarantee maximum enhancement performance. Again, future work could investigate methods which guarantee maximum enhancement performance.

Vibration in the optical setup prevents the identification of the linear phase difference between phase maps for adjacent CCD segments. Introducing vibration into the simulations obscured the linear phase difference present in the ideal simulations. The reconstruction method was still valid in this case and the reconstructed RM showed a substantial improvment in average enhancement when the reference phase-map enhancement was near η_{max} for the original RM.

An imaging system configuration for reflective inverse diffusion eliminates the need

to measure the entire RM. However, measuring the RM with parallel wavefront modulation is currently faster than previous single-point iterative optimization methods. Future research should investigate more sophisticated intensity-based phase-retrieval methods (*e.g.*, steepest descent, Gerchberg-Saxton, conjugate-gradient method) for single-segment optimizations. The phase maps for the remaining segments in the observation plane can be determined using phase tilts.

VII. Conclusion

The goal of this research was to develop a method of controlled illumination using reflected light that could be incorporated into the existing indirect-photography configuration to effectively reduce it to the much simpler dual-photography configuration to recover images around corners. The original reflective inverse diffusion research was a simple proof-of-concept experiment, with little mathematical background, and conducted under the assumption that the process operated similarly to transmissive inverse diffusion [38]. The analysis accomplished in this dissertation provided a mathematical basis for maximum expected enhancement for reflective inverse diffusion (see Chapter III). Diffraction theory led to the development of a fast-Fourier-transform-based simulation that can produce accurate enhancement results that take only minutes to complete versus the original experimental runtime of 10 hours (see Chapter III). This provides the means for efficient development of new reflective inverse diffusion techniques.

Reflection matrices (RMs) were developed in Chapter IV for reflective inverse diffusion based on parallel wavefront modulation [17, 19]. Initial attempts at measuring a RM from a rough-surface reflector demonstrated limitations of the original focal-plane optical setup shown in Figure 2. The process was moderately successful for the relatively smooth, specular, polished aluminum sample. RMs provide the necessary control of the reflected light for use as an illumination source in a dual photography system.

The initial RM measurements led to the development of the imaging-system optical setup in Figure 10 (see Chapter II). This setup is similar to that used in transmissive inverse diffusion, on which reflective inverse diffusion was modeled, but had been considered less practical in application for the reflective case. The enhancement performance of the two optical systems was compared against surface properties of

roughness, correlation length, and surface slope. Surface slope was determined to be the most significant parameter in regard to enhancement. The surface slope was used to define the lateral surface dimension ($\ell_{\lambda/2}$) for reflective inverse diffusion. The RM measurement time of approximately 5 minutes led to the discovery of minute vibrations in the optical system that significantly reduced the enhancement performance in laboratory experiments. When small random shifts were added to the rough-surface to model these vibrations, the simulation results aligned with laboratory experiments. The simulation capabilities have been continuously developed in both speed and accuracy. Low resolution simulations of the imaging system can now complete a RM measurement in as little as 30 seconds.

Finally, in Chapter VI, analysis of the RM measured by the imaging system revealed a linear phase tilt relationship between phase maps that target adjacent segments in the observation plane. The vibration noise that limited enhancement of the laboratory experiments also obscures these linear phase-pattern differences of the RMs measured in the laboratory. This relationship can be exploited to rebuild or expand an RM without requiring re-measurement. New RMs can be constructed from a single phase map with comparable and even improved enhancement performance. Since this process is linear, a similar relationship is expected for the focal-plane system using the inverse spatial Fourier transform of the tilt phasemaps in Figure 16. However, development of this relationship is left for future work. This capability will be needed for the intended application of imaging around corners. Using the imaging system, a RM can be constructed and then extended into an occluded, unmeasured portion of the scene. The scene is then illuminated using reflective inverse diffusion via the RM and the occluded scene can be imaged from the point of view of the reflective surface using dual photography [2].

7.1 Contributions

A collabortive effort with the previous AFIT masters student, Lieutenant Jessica Schafer (now Captain Jessica Ullom) [38, 42] who collected the original experimental reflective inverse diffusion data was combined with the corroborative mathematical foundation and simulation results presented in Chapter III to produced the first peer reviewed paper on the subject, "Reflective Inverse Diffusion," by Burgi, Ullom, Marciniak and Oxley. The paper has been accepted for publication in Applied Sciences [9].

The initial results in the development of RMs for reflective inverse diffusion discussed in Chapter IV was presented at the Optics and Photonics conference in San Diego, California in August 2016. The corresponding SPIE proceedings paper "Matrix methods for reflective inverse diffusion," by Burgi, Marciniak, Nauyoks and Oxley was published in SPIE Proceedings volume 9961 [43].

The matrix methods were expanded to include changes to the optical system and material surface properties that can affect enhancement performance of the RM in Chapter V. The paper "Measuring the reflection matrix of a rough surface," by Burgi, Marciniak, Nauyoks and Oxley has been submitted for publication in Optical Engineering and is currently under peer review [44].

A final paper, "Expansion of the Reflection Matrix of a Rough Surface," by Burgi, Marciniak, Nauyoks and Oxley, based on the work in Chapter VI is currently in preparation and targeted for submission to Optical Engineering.

7.2 Future Research

Further research is required to solidify the RM measurement method. Improving the vibration isolation of the optical system will be key to improving the RM enhancement performance. Mathematical methods for combating the effects of vibration, such

as dynamic data driven applications systems (DDDAS) [40], can now be explored as a more cost effective and suitable solution based on the intended application.

Development of an application-specific optical system should be pursued in the future to replace the simple single lens providing demagnification. Enhancement performance is expected to increase substantially with improved optics. An imaging system with greater levels of demagnification should improve enhancement performance for rough surfaces with smaller lateral surface dimensions ($\ell_{\lambda/2}$).

The substantial RMS phase difference between the measured RM and a the RM reconstructed from a single phase map, suggests multiple RMs exist for a given rough surface with comparable enhancement performances. The parallel wavefront modulation method used for measuring the RM should be examined more closely for the cause of the multiple solutions. Currently, the parallel wavefront modulation optimizes the intensity of a single observation-plane segment. Future research should also look for ways to optimize the RM measurement method to produce the maximum enhancement.

Also, currently, measurement of the RM requires less time and provides more information that iterative optimization techniques. However, with the linear phase relationship of the imaging system the RMs can be constructed around phase maps optimized with more sophisticated intensity-based phase-retrieval methods (*e.g.*, steepest descent, Gerchberg-Saxton, conjugate-gradient method) and should be examined for practical implementation in future research. The RM reconstruction methods for the focal-plane system based on the inverse 2-D spatial Fourier transform of the linear tilt phase map should be also be investigated in future work to determine its potential for use in the imaging-around-corners application.

The coherence length of the laser source may become a concern at the longer propagation distances given the intended application. The temporal coherence of the

light from each of the SLM segments decreases as the propagation distance exceeds the coherence length of the source. As the degree of coherence decreases, it will become increasingly difficult for the SLM to compensate for the surface height fluctuations of the reflector and produce a converging phase front after reflection. Currently available stabilized HeNe lasers have coherence lengths of several hundred meters.

There are significant device limitations to be overcome before reflective inverse diffusion can be incorporated into a system for imaging around corners. High-speed phase modulators are needed for the intended application. Dual photography requires 1024 intensity measurements to produce a single low-resolution 32×32 pixel image from reflected light [2]. Imaging a dynamic scene at just 1 frame-per-second would require a phase modulator with a frequency response of approximately 1 kHz, well beyond the the 30 Hz of the current LCoS SLMs. High speed phase modulators would also reduce the measurement time of the RM and make it less susceptible to the vibrational noise responsible lower than expected enhancement performance. However, these speeds would likely have to exceed 10's of kHz.

Appendix A. MATLAB® Source Code

A.1 Reflective Inverse Diffusion - Iterative Algorithm

The following MATLAB® code was use to simulate the original proof-of-concept experiments from Chapter II using the diffraction base model from Chapter III. The source code used to propagate the SLM to the observation plane is available in section A.3.1.

```
%% Propagation Simulations
lambda=633*10^-9;    % HeNe wavelength
k=2*pi/lambda;       % wavenumber

slmpix=512;          % number for physical SLM pixels
a=2;                 % zero-pad factor

D=0.00768;                          % physcial SLM side length
dx1=D/slmpix;                       % SLM delta-x
x1=((-slmpix/2):(slmpix/2-1))*dx1;  % SLM coordinate array
flens=0.5;                          % positive lens focal length
z1=0.15;                            % distance from the SLM to the lens
z2=0.5;                             % distance from the reflector to the CCD

dx2=lambda*flens/(a*D);                 % sample pixel size
x2=((-a*slmpix/2):(a*slmpix/2-1))*dx2;  % sample coordinate array

sample=exp(1i*2*pi*rand(a*slmpix));     % uniform distribution

CCDchannels=1024;               % total CCD segments
CCDdimension=sqrt(CCDchannels);

SLMchannels=1024;               % final number of optimized SLM segments
SLMdimension=sqrt(SLMchannels);

s1=1;s2=512;s3=s1;s4=s2;

%% Iterative Optimization to TestChannel
% start with random SLM segments
SLM1=ExpImage(exp(1i*2*pi*rand(slmpix)),[slmpix slmpix]);
TestChannel=(CCDdimension+1)*CCDdimension/2;    % select target channel
[ChannelMask,BackgroundMask]=ChannelMasks(TestChannel,CCDdimension,(s2-s1+1));
PhaseSpacing=16;    % number of tested phase values
PhaseValue=exp(1i*2*pi/PhaseSpacing*((-PhaseSpacing/2):(PhaseSpacing/2-1)));
kmax=log(SLMchannels)/log(4);   % calculate iterations of outer for loop

for k=1:kmax
    N=2^(2*k);  % number of segments to pre-optimize
    for n=1:N
        ChannelIntensity=zeros(length(PhaseValue),1);   % initializes intensity
        SLMmask=ChannelMasks(n,sqrt(N),slmpix);         % select SLM segment
        for p=1:length(PhaseValue)
```

```
            SLM1(SLMmask)=PhaseValue(p);                    % tested phase value
            % propagate to Obs plane
            Uobs=PropagateSLM(SLM1,z1,flens,z2,sample,a);
            Iobs=abs(Uobs(s1:s2,s3:s4)).^2;             % calculate intensity
            % save intensity
            ChannelIntensity(p)=sqrt(mean(Iobs(ChannelMask).^2));
        end
        [~,idx]=max(ChannelIntensity);  % determine maximum intensity
        SLM1(SLMmask)=PhaseValue(idx);  % set segment to phase value of max
    end
end
```

A.2 Reflective Inverse Diffusion - Matrix Method

A.2.1 Focal Plane Simulation.

The following MATLAB® code was use to simulate the measurement of the reflection matrix (RM) using the optical setup from Figure 2 with the rough surface reflector placed at the lens focus. The diffraction base model from Chapter III was used. The source code used to propagate the SLM to the observation plane is available in section A.3.1.

```
%% Propagation Simulations
lambda=633*10^-9;    % HeNe wavelength
k=2*pi/lambda;       % wavenumber

slmpix=512;          % number for physical SLM pixels
a=2;                 % zero-pad factor

D=0.00768;                          % physcial SLM side length
dx1=D/slmpix;                       % SLM delta-x
x1=((-slmpix/2):(slmpix/2-1))*dx1;  % SLM coordinate array
flens=0.5;                          % positive lens focal length
z1=0.15;                            % distance from the SLM to the lens
z2=0.5;                             % distance from the reflector to the CCD

dx2=lambda*flens/(a*D);                 % sample pixel size
x2=((-a*slmpix/2):(a*slmpix/2-1))*dx2;  % sample coordinate array

%% Random Sample
SampleDimension=2048;    % sample size in pixels
JitterSpace=0;           % magnitude of random shift
JitterOffset=1;          % offset center for random shift
% sample with uniform phase distribution
Jsample=exp(1i*2*pi*rand(SampleDimension+2*JitterSpace));

%% Device Error
CCDerror=0;         % intensity measurement error in percent
SLMerror=0;         % SLM error in radian
```

```
%% Parallel Wavefront Opt Variables
CCDchannels=128^2;  % total CCD segments
CCDdimension=sqrt(CCDchannels);
CCDmap=reshape(1:CCDchannels,CCDdimension,CCDdimension);

SLMchannels=1024; % total SLM segments
SLMdimension=sqrt(SLMchannels);
G=SLMchannels/2;
p=1:G;
w0=2*pi;            % 1 Hz frame per second
wp=(G+p)/(4*G)*w0;  % SLM segment frequencies

map1=flip((checkerboard(1,SLMdimension/2,SLMdimension/2)>0.5),2);
grp1=zeros(SLMdimension);
grp1(map1)=wp;  % group 1 checkboard of modulated and static segments

map2=(checkerboard(1,SLMdimension/2,SLMdimension/2)>0.5);
grp2=zeros(SLMdimension);
grp2(map2)=wp; % group 2 checkboard of modulated and static segments

%% Observation Plane Windowing
s1=129;s2=896;s3=s1;s4=s2;   % for standard 20.6 micro 768x768 obs plane
% s1=257;s2=1792;s3=s1;s4=s2; % for standard 10.3 1536x1536 obs plane

%% Initialize Reflection Matrix
Rm=zeros(CCDchannels,SLMchannels);

%% capture group 1
frames=zeros(CCDchannels,4*G);
for t=0:(4*G-1)
    SLMnoise=SLMerror*(2*rand(size(grp1))-1);
    SLM=ExpImage(exp(1i*quant(grp1*t+SLMnoise,2*pi/16384)),[slmpix slmpix]);

    % simulation optics table vibration
    Jx=randi(2*JitterSpace+1)-(JitterSpace+1);
    Jy=randi(2*JitterSpace+1)-(JitterSpace+1);
    JstartX=JitterSpace+Jx+JitterOffset;
    JstopX=JstartX+SampleDimension-1;
    JstartY=JitterSpace+Jy+JitterOffset;
    JstopY=JstartY+SampleDimension-1;
    sample=Jsample(JstartX:JstopX,JstartY:JstopY);

    [Uobs,Uminus,Uplus]=PropagateSLM(SLM,z1,flens,z2,sample,a);
    CCDnoise=CCDerror*(2*rand(size(Uobs(s1:s2,s1:s2)))-1)+1;
    Iobs=CCDnoise.*abs(Uobs(s1:s2,s3:s4)).^2;
    frames(:,t+1)=reshape(BinImage(Iobs,...
        [CCDdimension CCDdimension]),CCDchannels,1);
end

%% Extract Group 1 <ym|R>*tmp
fftgrp=zeros(size(frames));
```

```
hmap1=reshape(map1.',1,SLMchannels);
rmap1=logical(ones(CCDchannels,1)*map1(:).');
fftgrp=fft(frames,[],2);
Rm(rmap1)=fftgrp(:,(G+2):(2*G+1));

%% capture group 2 intensity patterns
frames=zeros(CCDchannels,4*G);
for t=0:(4*G-1)
    SLMnoise=SLMerror*(2*rand(size(grp2))-1);
    SLM=ExpImage(exp(1i*quant(grp2*t+SLMnoise,2*pi/16384)),[slmpix slmpix]);

    % simulation optics table vibration
    Jx=randi(2*JitterSpace+1)-(JitterSpace+1);
    Jy=randi(2*JitterSpace+1)-(JitterSpace+1);
    JstartX=JitterSpace+Jx+JitterOffset;
    JstopX=JstartX+SampleDimension-1;
    JstartY=JitterSpace+Jy+JitterOffset;
    JstopY=JstartY+SampleDimension-1;
    sample=Jsample(JstartX:JstopX,JstartY:JstopY);

    [Uobs,Uminus,Uplus]=PropagateSLM(SLM,z1,flens,z2,sample,a);
    CCDnoise=CCDerror*(2*rand(size(Uobs(s1:s2,s1:s2)))-1)+1;
    Iobs=CCDnoise.*abs(Uobs(s1:s2,s3:s4)).^2;
    frames(:,t+1)=reshape(BinImage(Iobs,...
        [CCDdimension CCDdimension]),CCDchannels,1);
end

%% Extract Group 2 <ym|R>*tmp
fftgrp=zeros(size(frames));
hmap2=reshape(map2.',1,SLMchannels);
rmap2=logical(ones(CCDchannels,1)*map2(:).');
fftgrp=fft(frames,[],2);
Rm(rmap2)=fftgrp(:,(G+2):(2*G+1));

%% capture group 3 intensity patterns
grp3=2*pi*(map1*(3/8)+map2*(4/8));
frames=zeros(CCDchannels,8);
for t=0:7
    SLMnoise=SLMerror*(2*rand(size(grp3))-1);
    SLM=ExpImage(exp(1i*quant(grp3*t+SLMnoise,2*pi/16384)),[slmpix slmpix]);

    % simulation optics table vibration
    Jx=randi(2*JitterSpace+1)-(JitterSpace+1);
    Jy=randi(2*JitterSpace+1)-(JitterSpace+1);
    JstartX=JitterSpace+Jx+JitterOffset;
    JstopX=JstartX+SampleDimension-1;
    JstartY=JitterSpace+Jy+JitterOffset;
    JstopY=JstartY+SampleDimension-1;
    sample=Jsample(JstartX:JstopX,JstartY:JstopY);

    [Uobs,Uminus,Uplus]=PropagateSLM(SLM,z1,flens,z2,sample,a);
    CCDnoise=CCDerror*(2*rand(size(Uobs(s1:s2,s1:s2)))-1)+1;
```

```
    Iobs=CCDnoise.*abs(Uobs(s1:s2,s3:s4)).^2;
    frames(:,t+1)=reshape(BinImage(Iobs,...
        [CCDdimension CCDdimension]),CCDchannels,1);
end

%% Calculate Compenstation Term from Group 3
fftgrp=zeros(size(frames));
fftgrp=fft(frames,[],2);
Ctemp=fftgrp(:,4).*fftgrp(:,5)./fftgrp(:,8)+fftgrp(:,4)+fftgrp(:,5)+fftgrp(:,8);
C=Ctemp./abs(Ctemp);
Cm=repmat(C,1,G);

%% Apply Compensation term
Rcomp=Rm;
Rcomp(rmap2)=Rcomp(rmap2).*Cm(:);
```

A.2.2 Image Plane Simulation.

The following MATLAB® code was used to simulate the measurement of the reflection matrix (RM) using the optical setup from Figure 10 with the rough surface reflector in an image plane of the SLM. The diffraction base model from Chapter III was used; however, equation (52) provided the output for the observation plane. The source code used to propagate the SLM to the observation plane is available in section A.3.2.

```
%% Propagation Simulations
lambda=633*10^-9;    % HeNe wavelength
k=2*pi/lambda;       % wavenumber
z1=0.5;      % distance from sample to CCD

%% Programmable variables
Demagnification=7.68;           % ideal demagnification of SLM
SLMdimension=32;                % SLM segments per side

%% Random Sample
SampleDimension=2048;    % sample size in pixels
JitterSpace=0;           % magnitude of random shift
JitterOffset=1;          % offset center for random shift
% sample with uniform phase distribution
Jsample=exp(1i*2*pi*rand(SampleDimension+2*JitterSpace));

CCDerror=0;                     % intensity measurement error in percent
SLMerror=0;                     % SLM error in radian

%% Virtual SLM
D=0.00768/Demagnification;      % SLM side length;

dx1=D/SLMdimension;             % SLM pixel size in meters
dx2=D/SampleDimension;          % pixel size in the observation plane
```

```
% Parallel Wavefront Optimization Parameters
SLMchannels=SLMdimension^2;        % Total SLM segments
G=SLMchannels/2;                   % SLM segments per group
p=1:G;                             % array counter
w0=2*pi;                           % 1 Hz frame per second sampling
wp=(G+p)/(4*G)*w0;                 % SLM segment frequencies

map1=flip((checkerboard(1,SLMdimension/2,SLMdimension/2)>0.5),2);
grp1=zeros(SLMdimension);
grp1(map1)=wp;  % group 1 checkboard of modulated and static segments

map2=(checkerboard(1,SLMdimension/2,SLMdimension/2)>0.5);
grp2=zeros(SLMdimension);
grp2(map2)=wp;  % group 2 checkboard of modulated and static segments

%% Observation plane windowing
if SampleDimension==32
    s1=25;s2=344;        % for sample 32x32
    ScanStep=1;
elseif SampleDimension==64
    s1=369;s2=1008;      % for sample 64x64
    ScanStep=1;
elseif SampleDimension==96
    s1=481;s2=2592;      % for sample 96x96
    ScanStep=1;
elseif SampleDimension==128
    s1=2049;s2=3328;      % for sample 128x128
    ScanStep=1;
else
    error('Unsupported SampleDimension')
end

CCDdimension=32;            % obs plane width in segments
CCDchannels=CCDdimension^2; % total number of CCD segments
CCDmap=reshape(1:CCDchannels,CCDdimension,CCDdimension);

%% Initialize Reflection Matrix
Rm=zeros(CCDchannels,SLMchannels);

%% capture group 1
frames=zeros(CCDchannels,4*G);
for t=0:(4*G-1)
    SLMnoise=SLMerror*(2*rand(size(grp1))-1);
    SLM=exp(1i*quant(grp1*t+SLMnoise,2*pi/16384));

    % simulation optics table vibration
    Jx=randi(2*JitterSpace+1)-(JitterSpace+1);
    Jy=randi(2*JitterSpace+1)-(JitterSpace+1);
    JstartX=JitterSpace+Jx+JitterOffset;
    JstopX=JstartX+SampleDimension-1;
    JstartY=JitterSpace+Jy+JitterOffset;
    JstopY=JstartY+SampleDimension-1;
```

```
    sample=Jsample(JstartX:JstopX,JstartY:JstopY);

    Uobs=PropSLMImage(SLM,D,sample,z1);
    CCDnoise=CCDerror*(2*rand(size(Uobs(s1:s2,s1:s2)))-1)+1;
    Iobs=CCDnoise.*abs(Uobs(s1:s2,s1:s2)).^2;
    frames(:,t+1)=reshape(BinImage(Iobs,...
        [CCDdimension CCDdimension]),CCDchannels,1);
end

%% Extract Group 1 <ym|R>*tmp
fftgrp=zeros(size(frames));
hmap1=reshape(map1.',1,SLMchannels);
rmap1=logical(ones(CCDchannels,1)*map1(:).');
fftgrp=fft(frames,[],2);
Rm(rmap1)=fftgrp(:,(G+2):(2*G+1));

%% capture group 2 intensity patterns
frames=zeros(CCDchannels,4*G);
for t=0:(4*G-1)
    SLMnoise=SLMerror*(2*rand(size(grp2))-1);
    SLM=exp(1i*quant(grp2*t+SLMnoise,2*pi/16384));

    % simulation optics table vibration
    Jx=randi(2*JitterSpace+1)-(JitterSpace+1);
    Jy=randi(2*JitterSpace+1)-(JitterSpace+1);
    JstartX=JitterSpace+Jx+JitterOffset;
    JstopX=JstartX+SampleDimension-1;
    JstartY=JitterSpace+Jy+JitterOffset;
    JstopY=JstartY+SampleDimension-1;
    sample=Jsample(JstartX:JstopX,JstartY:JstopY);

    Uobs=PropSLMImage(SLM,D,sample,z1);
    CCDnoise=CCDerror*(2*rand(size(Uobs(s1:s2,s1:s2)))-1)+1;
    Iobs=CCDnoise.*abs(Uobs(s1:s2,s1:s2)).^2;
    frames(:,t+1)=reshape(BinImage(Iobs,...
        [CCDdimension CCDdimension]),CCDchannels,1);
end

%% Extract Group 2 <ym|R>*tmp
fftgrp=zeros(size(frames));
hmap2=reshape(map2.',1,SLMchannels);
rmap2=logical(ones(CCDchannels,1)*map2(:).');
fftgrp=fft(frames,[],2);
Rm(rmap2)=fftgrp(:,(G+2):(2*G+1));

%% capture group 3 intensity patterns
grp3=2*pi*(map1*(3/8)+map2*(4/8));
frames=zeros(CCDchannels,8);
for t=0:7
    SLMnoise=SLMerror*(2*rand(size(grp3))-1);
    SLM=exp(1i*quant(grp3*t+SLMnoise,2*pi/16384));
```

```
    % simulation optics table vibration
    Jx=randi(2*JitterSpace+1)-(JitterSpace+1);
    Jy=randi(2*JitterSpace+1)-(JitterSpace+1);
    JstartX=JitterSpace+Jx+JitterOffset;
    JstopX=JstartX+SampleDimension-1;
    JstartY=JitterSpace+Jy+JitterOffset;
    JstopY=JstartY+SampleDimension-1;
    sample=Jsample(JstartX:JstopX,JstartY:JstopY);

    Uobs=PropSLMImage(SLM,D,sample,z1);
    CCDnoise=CCDerror*(2*rand(size(Uobs(s1:s2,s1:s2)))-1)+1;
    Iobs=CCDnoise.*abs(Uobs(s1:s2,s1:s2)).^2;
    frames(:,t+1)=reshape(BinImage(Iobs,...
        [CCDdimension CCDdimension]),CCDchannels,1);
end

%% Calculate Compenstation Term from Group 3
fftgrp=zeros(size(frames));
fftgrp=fft(frames,[],2);
Ctemp=fftgrp(:,4).*fftgrp(:,5)./fftgrp(:,8)+fftgrp(:,4)+fftgrp(:,5)+fftgrp(:,8);
C=Ctemp./abs(Ctemp);
Cm=repmat(C,1,G);

%% Apply Compensation term
Rcomp=Rm;
Rcomp(rmap2)=Rcomp(rmap2).*Cm(:);
```

A.3 SLM Propagation Functions

A.3.1 Focal Plane Optical System.

The following MATLAB® code was used to propagate the simulated SLM to the observation plane base on the focal plane optical setup in Figure 2 with the rough surface reflector placed at the lens focus. The diffraction base model from III was used. The propagation was based on equation (38).

```
% Uobs = observation plane
% Uminus = field just prior to reflection
% Uplux = field just after reflection
% dx3 = observation plane pixel size
% z1 = distance from SLM to Lens
% z2 = distance from Lens to Observation plane

function [Uobs,Uminus,Uplus,dx3] =
        PropagateSLM(input,z1,focus,z2,sample,a,recalc)

% persisent variable for computational efficiency
persistent prevZ1 prevF prevZ2 prevM prevN prevA
persistent x3 chirp dx1
persistent Hslm2lens Hsample2ccd
```

```
if nargin<7
    recalc=0;
elseif nargin<6
    a=2;
    recalc=0;
elseif nargin<5
    sample=1;
    a=2;
    recalc=0;
end

[m,n]=size(input);
M=a*m;

[msample,nsample]=size(sample);
if msample~=1 || nsample~=1
    if a*m~=msample && a*n~=nsample
        error('sample incorrect size')
    end
end

% check for changes that require recalculation of persistent variables
if isempty(prevZ1)
    recalc=1;
    prevZ1=0;
    prevF=0;
    prevZ2=0;
    prevM=0;
    prevN=0;
    prevA=0;
elseif z1~=prevZ1 || focus~=prevF ||...
        z2~=prevZ2 || m~=prevM || n~=prevN || a~=prevA
    recalc=1;
end

if recalc
    display('recalculating');

    lambda=633*10^-9;
    k=2*pi/lambda;
    D=0.00768;              % SLM dimension

    L1=a*D;

    % slm plane coordinates
    dx1=L1/M;                       % SLM pixel size
    x1=-L1/2:dx1:L1/2-dx1;
    [X1,Y1]=meshgrid(x1);

    % propagation TF - SLM to Lens
    fx2=(-M/2:M/2-1)*1/L1;
```

```
    [FX2,FY2]=meshgrid(fx2);
    Hslm2lens=exp(1i*k*z1*sqrt(1-(lambda*FX2).^2-(lambda*FY2).^2));

    % sample plane coordinates
    dx3=lambda*focus/L1;
    L3=lambda*focus/dx1;
    x3=-L3/2:dx3:L3/2-dx3;
    [X3,Y3]=meshgrid(x3);
    % Fraunhofer chirp
    chirp=exp(1i*k/(2*focus)*(X3.^2+Y3.^2));

    % propagation TF - sample to CCD
    fx4=(-M/2:M/2-1)*1/L3;
    [FX4,FY4]=meshgrid(fx4);
    Hsample2ccd=exp(1i*k*z2*sqrt(1-(lambda*FX4).^2-(lambda*FY4).^2));

    prevZ1=z1;
    prevF=focus;
    prevZ2=z2;
    prevM=m;
    prevN=n;
    prevA=a;
end

u1=padarray(input,[(M-m)/2,(M-m)/2]);
Uminus=chirp.*fftshift(fft2(fftshift(u1)))*dx1^2.*Hslm2lens;
Uplus=sample.*Uminus;
Uobs=fftshift(ifft2(fft2(fftshift(Uplus)).*fftshift(Hsample2ccd)));
end
```

A.3.2 Image Plane Optical System.

The following MATLAB® code was used to propagate the simulated SLM to the observation plane base on the imaging system optical in Figure 10 with the rough surface reflector placed is the imaging plane of the SLM. The diffraction base model from III was used. The propagation was based on equation (52).

```
% ObsOut = observation plane
% z1 = distance from sample to Observation plane

function [ObsOut] = PropSLMImage(SLM1,SLMdim,sample,PropZ,recalc)

% persistent variables for computational efficiency
persistent pad pSLMdim pZ Hsample2ccd
persistent pSx pSLMx

[SLMx,SLMy]=size(SLM1);
[Sx,Sy]=size(sample);

if nargin<5
```

```
    recalc=0;   % default use previous Hsample2ccd values
end
if isempty(Hsample2ccd)
    recalc=1;
elseif SLMdim~=pSLMdim || PropZ~=pZ || Sx~=pSx || SLMx~=pSLMx
    recalc=1;
end

if mod(Sx,SLMx)~=0 || mod(Sy,SLMy)~=0
    error('sample size not multiple of SLM')
elseif Sx~=Sy || SLMx~=SLMy
    error('sample or SLM not square')
elseif mod(SLMx,2)~=0 || mod(Sx,2)~=0
    error('even samples only')
end

if recalc
    lambda=633*10^-9;
    k=2*pi/lambda;

    if Sx==32
        pixout=368;
    elseif Sx==64
        pixout=1376;
    elseif Sx==96
        pixout=3072;
    elseif Sx==128
        pixout=5376;
    else
        error('Unsupported Sample Size');
    end

    % side length of demagnified zero padded SLM image
    L1=pixout*(SLMdim/Sx);

    fx=(-pixout/2:pixout/2-1)*1/L1;
    [FX,FY]=meshgrid(fx);
    % Rayleigh-Sommerfeld Transfer Function
    Hsample2ccd=exp(1i*k*PropZ*sqrt(1-(lambda*FX).^2-(lambda*FY).^2));
    % Fresnel Transfer Function
    %Hsample2ccd=exp(-1i*pi*lambda*PropZ*(FX.^2+FY.^2));

    pad=(pixout-Sx)/2;                  % pad output
    pSLMdim=SLMdim;
    pZ=PropZ;
    pSx=Sx;
    pSLMx=SLMx;
end

u1=padarray(sample.*ExpImage(SLM1,[Sx Sy]),[pad pad]);
ObsOut=fftshift(ifft2(fft2(fftshift(u1)).*fftshift(Hsample2ccd)));
end
```

Bibliography

1. M. Born and E. Wolf, *Principles of optics: electromagnetic theory of propagation, interference and diffraction of light*, Cambridge university press, 1999.

2. P. Sen, B. Chen, G. Garg, S. R. Marschner, M. Horowitz, M. Levoy, and H. Lensch, "Dual photography," in *ACM Transactions on Graphics (TOG)*, **24**(3), pp. 745–755, ACM, 2005.

3. M. G. Hoelscher, *Restoration of Scene Information Reflected from Non-Specular Media*. PhD dissertation, Air Force Institute of Technology, 2011.

4. M. G. Hoelscher and M. A. Marciniak, "Restoration of scene information reflected from a non-specular surface," in *SPIE Optical Engineering+ Applications*, pp. 77920L–77920L, International Society for Optics and Photonics, 2010.

5. I. Vellekoop and A. Mosk, "Focusing of light by random scattering," *arXiv preprint cond-mat/0604253* , 2006.

6. I. M. Vellekoop and A. Mosk, "Focusing coherent light through opaque strongly scattering media," *Optics letters* **32**(16), pp. 2309–2311, 2007.

7. I. Vellekoop and A. Mosk, "Phase control algorithms for focusing light through turbid media," *Optics Communications* **281**(11), pp. 3071–3080, 2008.

8. I. M. Vellekoop, "Controlling the propagation of light in disordered scattering media," *arXiv preprint arXiv:0807.1087* , 2008.

9. K. Burgi, J. Ullom, M. Marciniak, and M. Oxley, "Reflective inverse diffusion," *Applied Sciences* **6**(12), p. 370, 2016.

10. J. W. Goodman, *Speckle phenomena in optics: theory and applications*, Roberts and Company Publishers, 2007.

11. J. C. Stover, *Optical scattering: measurement and analysis*, vol. 2, SPIE optical engineering press Bellingham, WA, 1995.

12. I. M. Vellekoop, "Controlling the propagation of light in disordered scattering media," *arXiv preprint arXiv:0807.1087* , 2008.

13. J. W. Goodman, *Statistical optics*, John Wiley & Sons, 2000.

14. D. B. Conkey, A. M. Caravaca-Aguirre, and R. Piestun, "High-speed scattering medium characterization with application to focusing light through turbid media," *Optics express* **20**(2), pp. 1733–1740, 2012.

15. S. Popoff, G. Lerosey, M. Fink, A. C. Boccara, and S. Gigan, "Controlling light through optical disordered media: transmission matrix approach," *New Journal of Physics* **13**(12), p. 123021, 2011.

16. E. Tajahuerce, V. Durán, P. Clemente, E. Irles, F. Soldevila, P. Andrés, and J. Lancis, "Image transmission through dynamic scattering media by single-pixel photodetection," *Optics express* **22**(14), pp. 16945–16955, 2014.

17. J. Yoon, K. Lee, J. Park, and Y. Park, "Measuring optical transmission matrices by wavefront shaping," *Optics Express* **23**(8), pp. 10158–10167, 2015.

18. I. Vellekoop, A. Lagendijk, and A. Mosk, "Exploiting disorder for perfect focusing," *Nature Photonics* **4**(5), pp. 320–322, 2010.

19. M. Cui, "A high speed wavefront determination method based on spatial frequency modulations for focusing light through random scattering media," *Optics express* **19**(4), pp. 2989–2995, 2011.

20. C. Jin, R. R. Nadakuditi, E. Michielssen, and S. C. Rand, "Backscatter analysis based algorithms for increasing transmission through highly scattering random media using phase-only-modulated wavefronts," *JOSA A* **31**(8), pp. 1788–1800, 2014.

21. S. Popoff, G. Lerosey, R. Carminati, M. Fink, A. Boccara, and S. Gigan, "Measuring the transmission matrix in optics: an approach to the study and control of light propagation in disordered media," *Physical review letters* **104**(10), p. 100601, 2010.

22. Z. Shi, M. Davy, and A. Z. Genack, "Statistics and control of waves in disordered media," *Optics express* **23**(9), pp. 12293–12320, 2015.

23. A. Drémeau, A. Liutkus, D. Martina, O. Katz, C. Schülke, F. Krzakala, S. Gigan, and L. Daudet, "Reference-less measurement of the transmission matrix of a highly scattering material using a dmd and phase retrieval techniques," *Optics express* **23**(9), pp. 11898–11911, 2015.

24. H. Jang, C. Yoon, E. Chung, W. Choi, and H.-N. Lee, "Speckle suppression via sparse representation for wide-field imaging through turbid media," *Optics express* **22**(13), pp. 16619–16628, 2014.

25. W. Harm, C. Roider, A. Jesacher, S. Bernet, and M. Ritsch-Marte, "Lensless imaging through thin diffusive media," *Optics express* **22**(18), pp. 22146–22156, 2014.

26. O. Katz, E. Small, Y. Guan, and Y. Silberberg, "Noninvasive nonlinear focusing and imaging through strongly scattering turbid layers," *Optica* **1**(3), pp. 170–174, 2014.

27. M. Kim, W. Choi, Y. Choi, C. Yoon, and W. Choi, "Transmission matrix of a scattering medium and its applications in biophotonics," *Optics Express* **23**(10), pp. 12648–12668, 2015.

28. T. Kohlgraf-Owens and A. Dogariu, "Finding the field transfer matrix of scattering media," *Optics express* **16**(17), pp. 13225–13232, 2008.

29. S. R. Huisman, T. J. Huisman, T. A. Wolterink, A. P. Mosk, and P. W. Pinkse, "Programmable multiport optical circuits in opaque scattering materials," *Optics express* **23**(3), pp. 3102–3116, 2015.

30. J. Aulbach, B. Gjonaj, P. M. Johnson, A. P. Mosk, and A. Lagendijk, "Control of light transmission through opaque scattering media in space and time," *Physical review letters* **106**(10), p. 103901, 2011.

31. S.-M. Reijn, F. A. Pinheiro, D. Geskus, and N. U. Wetter, "Enabling focusing around the corner in multiple scattering media," *Applied Optics* **54**(25), pp. 7740–7746, 2015.

32. A. P. Mosk, A. Lagendijk, G. Lerosey, and M. Fink, "Controlling waves in space and time for imaging and focusing in complex media," *Nature photonics* **6**(5), pp. 283–292, 2012.

33. I. M. Vellekoop, "Feedback-based wavefront shaping," *Optics express* **23**(9), pp. 12189–12206, 2015.

34. H. Yılmaz, W. L. Vos, and A. P. Mosk, "Optimal control of light propagation through multiple-scattering media in the presence of noise," *Biomedical optics express* **4**(9), pp. 1759–1768, 2013.

35. J. W. Goodman, *Introduction to Fourier optics*, Roberts and Company Publishers, 2005.

36. D. G. Voelz, *Computational fourier optics: a MATLAB tutorial*, SPIE Press Bellingham, 2011.

37. I. Freund, "Looking through walls and around corners," *Physica A: Statistical Mechanics and its Applications* **168**(1), pp. 49–65, 1990.

38. J. M. Schafer and M. A. Marciniak, "The focusing of light scattered from diffuse reflectors using phase modulation," in *Proc. of SPIE Vol*, **8495**, pp. 84950O–84950O–17, 2012.

39. O. Katz, E. Small, and Y. Silberberg, "Looking around corners and through thin turbid layers in real time with scattered incoherent light," *Nature photonics* **6**(8), pp. 549–553, 2012.

40. F. Darema, "Dynamic data driven applications systems: New capabilities for application simulations and measurements," in *International Conference on Computational Science*, pp. 610–615, Springer, 2005.

41. J. D. Schmidt, "Numerical simulation of optical wave propagation with examples in matlab," SPIE Washington, 2010.

42. J. Schafer, "The focusing of light scattered from diffuse reflectors using phase modulation," Master's thesis, Air Force Institute of Technology, 2012.

43. K. W. Burgi, M. A. Marciniak, S. E. Nauyoks, and M. E. Oxley, "Matrix methods for reflective inverse diffusion," in *SPIE Optical Engineering+ Applications*, pp. 99610O–99610O, International Society for Optics and Photonics, 2016.

44. K. W. Burgi, M. A. Marciniak, S. E. Nauyoks, and M. E. Oxley, "Measuring the reflection matrix of a rough surface," *Optical Engineering* , 2016. Submitted for publication.

REPORT DOCUMENTATION PAGE

Form Approved
OMB No. 0704–0188

1. REPORT DATE (DD–MM–YYYY)	2. REPORT TYPE	3. DATES COVERED *(From — To)*
22-12-2016	PhD Dissertation	Jan 2014 – Dec 2016

4. TITLE AND SUBTITLE

Reflection Matrix Method for Controlling Light After Reflection From a Diffuse Scattering Surface

5a. CONTRACT NUMBER

5b. GRANT NUMBER

5c. PROGRAM ELEMENT NUMBER

6. AUTHOR(S)

Burgi, Kenneth W., Maj, USAF

5d. PROJECT NUMBER

5e. TASK NUMBER

5f. WORK UNIT NUMBER

7. PERFORMING ORGANIZATION NAME(S) AND ADDRESS(ES)
Air Force Institute of Technology
Graduate School of
2950 Hobson Way
WPAFB OH 45433-7765

8. PERFORMING ORGANIZATION REPORT NUMBER

AFIT-ENP-DS-16-D-011

9. SPONSORING / MONITORING AGENCY NAME(S) AND ADDRESS(ES)

Department of Engineering Physics
2950 Hobson Way
WPAFB OH 45433-7765
DSN 785-3636, COMM 937-255-3636

10. SPONSOR/MONITOR'S ACRONYM(S)
AFIT/ENP

11. SPONSOR/MONITOR'S REPORT NUMBER(S)

12. DISTRIBUTION / AVAILABILITY STATEMENT
Distribution Statement A: Approved for Public Release; Distribution Unlimited.

13. SUPPLEMENTARY NOTES

14. ABSTRACT

This research focuses on reflective inverse diffusion, which was a proof-of-concept experiment that used phase modulation to shape the wavefront of a laser causing it to refocus after reflection from a rough surface. By refocusing the light, reflective inverse diffusion has the potential to eliminate the complex radiometric model of indirect photography by creating a virtual light source at the first diffuse reflector that satisfies the line-of-sight requirement of dual photography. However, the initial reflective inverse diffusion experiments provided no mathematical background and were conducted under the premise that the process operated similarly to transmissive inverse diffusion.

In this research, diffraction modeling of the reflective inverse diffusion experiments led to the development of Fourier transform-based simulations. Simulations and experimentation were used to develop reflection matrix methods that determine the proper phase modulation to refocus light after reflection to any location in the observation plane. These techniques provide a new method for controlled illumination of an occluded scene that can be used in conjunction with dual photography. This document provides the mathematical background for reflective inverse diffusion, the reflection matrix methods for phase modulation, and describes the simulations and experiments conducted.

15. SUBJECT TERMS
Reflective Inverse Diffusion, Indirect Photography, Dual Photography, Reflective Scattering

16. SECURITY CLASSIFICATION OF			17. LIMITATION OF ABSTRACT	18. NUMBER OF PAGES	19a. NAME OF RESPONSIBLE PERSON
a. REPORT	b. ABSTRACT	c. THIS PAGE			Dr. Michael A. Marciniak, AFIT/ENP
U	U	U	UU	110	19b. TELEPHONE NUMBER (Include Area Code) (937) 255-3636 x4529, michael.marciniak@afit.edu